Journal of Computational Physics 545 (2026) 114449

Contents lists available at ScienceDirect

Journal of Computational Physics

journal homepage: www.elsevier.com/locate/jcp

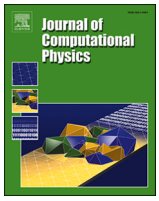

An unstructured high-order finite-volume scheme for the simulation of reactive multi-species flows

Florian Setzwein *, Peter Ess[1], Peter Gerlinger[2]

German Aerospace Center (DLR), Institute of Combustion Technology, Stuttgart, 70569, Germany

ARTICLE INFO

Keywords:
High-order discretization
Finite-volume method
Unstructured grids
Fractional step methods
Variable-density reacting flows in low Mach number regime
K-exact discretization schemes

ABSTRACT

In this work, a high-order finite-volume method is combined with an iterative projection approach to solve transport equations for reactive fluids in the low-Mach number regime. The proposed solution algorithm is fully collocated in both space and time and employs a vertex-centered k-exact discretization to achieve truly third-order spatial accuracy, even on fully unstructured median-dual grids. To enhance both accuracy and robustness, viscous and convective fluxes are treated consistently within the high-order framework. Convective fluxes are discretized using a central face-value approximation augmented with adaptive numerical dissipation control, governed by a novel gradient-limiting strategy that selectively reduces the order of accuracy near strong gradients while minimizing artificial dissipation elsewhere. The performance of the method is assessed against a conventional finite-volume scheme for unstructured grids, with a focus on reducing the number of computational elements required for accurate simulations. Benchmark test cases include the isochoric advection of a hydrogen-oxygen mixture, convection of a pseudo-isentropic vortex, and flame kernel–vortex interaction. As a key extension, a large-eddy simulation of a turbulent hydrogen/nitrogen-air diffusion flame on a fully unstructured three-dimensional grid is presented, demonstrating the method's capability to handle complex variable-density reactive flows in practical combustion scenarios. Results show that the k-exact scheme achieves accurate predictions even on relatively coarse grids, substantially reducing computational cost while maintaining physical fidelity - underscoring its potential for reactive flow simulations in both industrial and research applications.

1. Introduction

High-order schemes for unstructured grids offer significant potential for reducing computation time in detailed simulations of transient flows while maintaining substantial geometric flexibility in the mesh generation process [1]. In particular simulations that address reactive, multi-species flow problems benefit from a higher order accuracy, compared to conventional low-order schemes. This is due to the fact, that the computational overhead for achieving a higher accuracy in convective and diffusive transport is outweighed by the time-consuming evaluation of chemical source terms and mixture properties. Integrating high-order schemes into established unstructured finite-volume flow solvers, which often include numerous complex models, is a challenging task and requires significant verification and validation efforts. A promising approach to address these challenges is the k-exact multiple-correction

* Corresponding author.
E-mail address: florian.setzwein@dlr.de (F. Setzwein).
[1] Postdoctoral fellow.
[2] Professor.

https://doi.org/10.1016/j.jcp.2025.114449
Received 26 February 2025; Received in revised form 10 August 2025; Accepted 10 October 2025
Available online 15 October 2025

method [2,3], which enables a high-order reconstruction through successive corrections of approximate Green-Gauss derivatives with favorable parallel scaling properties and reasonable implementation effort. The cell-centered k-exact multiple-correction approach has recently been extended to vertex-centered median-dual grids within the framework of DLR's ThetaCOM (**T**urbulent **H**eat Release Extension for **TA**U in its **Com**bustion Version) flow solver. The scheme has been combined with a projection method to integrate the incompressible Navier-Stokes equations and it has been demonstrated, that it is capable of reducing the computing time for a wide range of both laminar and turbulent incompressible test cases, compared to conventional low-order finite-volume schemes [4–8].

In this work, we use the vertex-centered k-exact multiple-correction approach in conjunction with an iterative projection method for solving the conservation equations for variable-density reacting flows in the low Mach number regime. The latter are solved to overcome the stringent time step limitation in combustion problems, which primarily stems from the propagation of fast acoustic waves [9]. Neglecting acoustic effects opens the opportunity to decompose the pressure into a uniform thermodynamic component and a spatially fluctuating hydrodynamic component [10], which finally leads the system of equations to be separated into distinct solution steps. However, neglecting effects of compressibility induces an elliptical character in the system of equations, which, in addition to the numerical stiffness introduced by the reactive source terms, necessitates the use of implicit time-stepping schemes. This implicit treatment and the splitting of the solution process into distinct sub-steps introduces additional complexities for the extension of spatial discretization schemes to higher orders of accuracy, as these are typically combined with explicit time-stepping methods. In contrast to incompressible solution methods, density variations must be taken into account in combustion problems, which increases the thermodynamic coupling between the transported variables and requires a carefully structured solution strategy. A notable challenge in such systems is the appearance of spurious checkerboard oscillations, particularly when employing collocated grid arrangements. To mitigate these instabilities, temporal staggering of field variables is used commonly [11–18] , providing enhanced stability for the pressure-velocity coupling. Additionally, thermochemical transport equations are often formulated in a non-conservative manner [13,19–23] to reduce their dependence on density, thereby simplifying their numerical treatment. To increase stability for high density gradients, the nonlinear system of equations must be solved via iterative approaches [13,16–18], predictor-corrector methods [13,19,20,22] or formulations for the pressure-correction involving Poisson equations with variable coefficients [13,21,23,24].

Despite these challenges, several groups managed to develop fractional step schemes for reactive variable-density problems in conjunction with high-order accuracy. However, many of these efforts prioritize temporal accuracy, while relying on either conventional unstructured finite-volume schemes or structured high-order methods for spatial discretization. For example, Desjardins et al. [25] extended a high-order conservative finite-difference scheme to simulate variable-density flows using structured grids. Their method achieved up to sixth-order spatial accuracy and employed an iterative fractional step approach with temporal staggering, attaining second-order accuracy in time. Trisjono et al. [26] adapted this approach for simulating reactive flows. Motheau and Abraham [24] proposed an algorithm based on an operator-splitting strategy for the temporal integration of the low Mach number conservation equations with variable-density. Their approach relied on an implicit treatment of chemistry, while the advection-diffusion operators were handled using a Runge–Kutta–Chebyshev method. High-order compact schemes on structured grids were employed for the spatial discretization. Hassanaly et al. [27] developed a collocated solution procedure within the unstructured finite-volume solver OpenFOAM, focusing on a discretization that minimizes kinetic energy dissipation. Their method used a staggered arrangement of variables in time, second-order accuracy for the numerical flux discretization in space, and second-order temporal accuracy. Cang and Wang [28] introduced a semi-implicit algorithm that utilized collocated variables and formulated a Helmholtz equation for the pressure correction step. This algorithm was incorporated into a second-order accurate, cell-centered, unstructured finite-volume method. Reuter et al. [10] implemented an explicit, second-order accurate method for solving the low-Mach number variable-density equations in a pseudospectral solver. Their approach focused on resolving the redundancy between the mass conservation equation, the equation of state, and scalar transport equations, ensuring stability of the temporal discretization. This allowed for stable simulations with high density ratios up to 25.7.

This work builds upon the fractional step method by Pierce and Moin [16,29], who introduced an algorithm for solving the conservation equations for variable-density reactive flows in the low Mach number regime, utilizing structured grids with a staggered arrangement of variables in both space and time. Shunn et al. [30,31] later extended this approach to unstructured grids, adopting a collocated arrangement of variables in space while maintaining a staggered arrangement in time. Their method is characterized by an iterative solution of the conservation equations at each time level to enhance stability and reduce splitting errors [31]. This iterative approach achieves second-order temporal accuracy when at least two outer iterations are employed. Although additional iterations may improve the stability, they do not increase the order of accuracy [16,31]. In this work we extend the solution algorithm of Pierce and Moin [16,29] by applying the k-exact reconstruction framework, utilizing a collocated arrangement of field variables in both space and time. Our current 2-exact implementation enables spatial reconstruction of field variables with up to third-order accuracy, even on fully unstructured median-dual grids [4]. Convective fluxes are computed with third order spatial accuracy on truly unstructured grids, using a central flux formulation designed to minimize numerical dissipation [5]. This formulation is based on a stability equation derived from a von Neumann analysis of the discretization scheme. In this work, the method is combined with a gradient limitation strategy to effectively constrain thermochemical field variables. For diffusive fluxes, we employ a k-exact formulation of the face-tangent scheme [32,33], which has been shown to correspond to the well-known α-damping scheme [34] in recent studies [35], achieving second-order spatial accuracy on fully unstructured computational grids. The governing equations are solved sequentially in a fully implicit manner using a Crank-Nicolson scheme, which ensures low dissipation and second-order accuracy in time. Additionally, a deferred-correction approach is employed to accelerate the implicit calculation of high-order reconstructed fluxes and the chemical source terms, maintaining computational efficiency without sacrificing accuracy.

In the following sections, we present the solution algorithm and the k-exact discretization approach in detail. Subsequently, we describe the integration of these methods for solving the reactive conservation equations in the low Mach number regime, employing a collocated arrangement of field variables in both space and time. Special emphasis is placed on analyzing the spatial discretization error and deriving dedicated correction terms to enhance spatial accuracy. Furthermore, we demonstrate how the calculation of reconstructed fluxes can be efficiently implemented using the deferred-correction approach, resulting in an implicit calculation scheme that improves both accuracy and computational efficiency. The proposed approach has been implemented in DLR's flow solver ThetaCOM, which is built upon the DLR TAU code, demonstrating the method's capability for seamless integration into established finite-volume flow solvers. The enhanced accuracy of our approach is demonstrated through various test cases of increasing complexity, with a focus on reconstruction levels $k = 1$ and $k = 2$. For comparison, a conventional unstructured finite-volume scheme is employed to assess both the accuracy improvements and the associated computational cost. The test cases include the convective transport of an isochoric H_2/O_2 mixture in $1D$, the convection of a pseudo-isentropic vortex on a two-dimensional grid of distorted triangles, a premixed flame kernel-vortex interaction in $2D$ and a large-eddy simulation of a turbulent H_2/N_2-air flame on a fully unstructured grid in $3D$.

2. Numerical methods

2.1. Governing equations

We solve the transport equations for reactive fluids in the low-Mach number regime, which are given by

$$\frac{\partial \rho}{\partial t} + \frac{\partial}{\partial x_i}\left(\rho u_i\right) = 0, \tag{1a}$$

$$\frac{\partial}{\partial t}\left(\rho u_i\right) + \frac{\partial}{\partial x_j}\left(\rho u_i u_j\right) = \frac{\partial \tau_{ij}}{\partial x_j} - \frac{\partial p}{\partial x_i}, \tag{1b}$$

$$\frac{\partial}{\partial t}\left(\rho Y_s\right) + \frac{\partial}{\partial x_i}\left(\rho u_i Y_s\right) = -\frac{\partial j_{i,s}}{\partial x_i} + \dot{\omega}_s, \tag{1c}$$

$$\frac{\partial}{\partial t}(\rho h) + \frac{\partial}{\partial x_i}\left(\rho u_i h\right) = -\frac{\partial q_i}{\partial x_i}. \tag{1d}$$

These equations are derived from the reactive transport equations of reactive fluids in compressible formulation by an asymptotic investigation towards small Mach numbers [19,36–39]. The system of equations is solved for the velocity components u_i, the hydrodynamic pressure p, the enthalpy h and $N_s - 1$ mass fractions Y_s. The last species is calculated from Dalton's law via summation $\sum Y_s = 1$ over all N_s species. The chemical source term $\dot{\omega}_s$ balances the formation and decomposition of a species s as a result of chemical reaction. Temperature T and density ρ are related to the thermodynamic pressure component p_0 using the ideal gas law $\rho = p_0 M/(R_u T)$ with the molecular weight $M = 1/(\sum_{s=1}^{N_s} Y_s/M_s)$ of the gas mixture and the universal gas constant R_u. Compared to the hydrodynamic pressure component p, the thermodynamic pressure p_0 remains spatially uniform. Both components are derived from the total pressure in the low-Mach number limit, where acoustic effects are neglected. The specific enthalpy of the mixture $h = \sum_{s=1}^{N_s} h_s Y_s$ is determined from specific enthalpies h_s of the pure substances, which in turn are calculated from NASA polynomials [40]. The latter provide temperature-dependent coefficients for accurately modeling the thermodynamic properties of individual species in the mixture. The shear stress tensor τ_{ij} describes the diffusive momentum transport due to frictional effects and it is modelled using Stokes' friction law

$$\tau_{ij} = \mu\left(2S_{ij} - \delta_{ij}\frac{2}{3}\frac{\partial u_k}{\partial x_k}\right) \qquad \text{with} \qquad S_{ij} = \frac{1}{2}\left(\frac{\partial u_i}{\partial x_j} + \frac{\partial u_j}{\partial x_i}\right), \tag{2}$$

where S_{ij} defines the shear stress tensor and μ is the dynamic viscosity. The heat flux q_i and the diffusive flux $j_{i,s}$ of a chemical component s are calculated by

$$q_i = -\frac{\lambda}{c_p}\frac{\partial h}{\partial x_i} \qquad \text{and} \qquad j_{i,s} = -\rho D_s \frac{\partial Y_s}{\partial x_i}. \tag{3}$$

The modeling of diffusive transport requires the calculation of the dynamic viscosity μ, the thermal conductivity λ, the heat capacity at constant pressure c_p and the diffusivity D_s of a species s, which are calculated as weighted averages of the pure gas properties [41,42].

The finite rate chemistry approach is used to model the chemical source term $\dot{\omega}_s$, where the conversion of reactants into products is described by a reaction mechanism involving N_r elementary reactions. The latter are expressed in a generalized way, where the conversion of a chemical species $\mathcal{R}_s$ due to a reversible reaction r is expressed by the following generalized reaction equation

$$\sum_{s=1}^{N_s} \nu'_{s,r}\mathcal{R}_s \underset{k_{b,r}}{\overset{k_{f,r}}{\rightleftharpoons}} \sum_{s=1}^{N_s} \nu''_{s,r}\mathcal{R}_s \qquad \text{with} \qquad r = 1, 2, \dots, N_r, \tag{4}$$

where $\mathcal{R}_s$ indicates the chemical component of species s. $\nu'_{s,r}$ and $\nu''_{s,r}$ denote the stoichiometric coefficients of the reactants and products. $k_{f,r}$ and $k_{b,r}$ represent temperature-dependent forward and backward reaction rates, that are calculated with a modified

Arrhenius approach. For a detailed description on the calculation of $k_{f,r,}$ and $k_{b,r}$ and their implementation, we refer to the literature [42–44]. The species source term $\dot{\omega}_s$ results from relating the species conversion rates to the reaction rates and the species concentration $c_s = \rho Y_s / M_s$ and balancing over all considered reactions

$$\dot{\omega}_s = M_s \sum_{r=1}^{N_r} \left(\nu''_{s,r} - \nu'_{s,r} \right) \left[k_{f,r} \prod_{t=1}^{N_s+1} c_t^{\nu'_{t,r}} - k_{b,r} \prod_{t=1}^{N_s+1} c_t^{\nu''_{t,r}} \right]. \tag{5}$$

2.2. Temporal discretization

This section describes the iterative projection method for solving the transport Eq. (1). In this description, ϕ^n represents the known solution at the current time step t_n, while ϕ^m denotes the intermediate solution obtained during the mth sub-iteration of the projection step. The goal is to iteratively refine ϕ^m until the solution ϕ^{n+1} at the next time step is determined, which corresponds to the new time level t_{n+1}. This approach ensures that ϕ^{n+1} satisfies the governing equations at t_{n+1}, with each sub-iteration progressively improving the accuracy and stability of the solution.

At the start of a new time step, all dependent field variables are synchronized with the current solution. This includes the variables μ^n, λ^n, c_p^n, D^n, as well as the Jacobian of the chemical source term, which is required for the semi-implicit calculation of $\dot{\omega}_s$. Next, the explicit fluxes and source terms of all transport equations are calculated and stored as right-hand sides RHS:

$$RHS_h = \frac{\rho^n h^n}{\Delta t} - \frac{1}{2} \frac{\partial}{\partial x_i} \left(\dot{m}_i^n h^n - q_i^n \right), \tag{6a}$$

$$RHS_{Y_s} = \frac{\rho^n Y_s^n}{\Delta t} - \frac{1}{2} \frac{\partial}{\partial x_i} \left(\dot{m}_i^n Y_s^n - j_{i,s}^n \right) + \frac{1}{2} \dot{\omega}_s^n, \tag{6b}$$

$$RHS_{u_i} = \frac{\rho^n u_i^n}{\Delta t} - \frac{1}{2} \frac{\partial}{\partial x_j} \left(\dot{m}_j^n u_i^n - \tau_{ij}^n \right) - \frac{\partial p^n}{\partial x_i}, \tag{6c}$$

where the mass fluxes $\dot{m}_i^n = \rho^n u_i^n$ have been introduced for the sake of clarity. The factors of $1/2$ arise due to the Crank-Nicolson scheme [45] for the temporal integration of convective and diffusive fluxes and the chemical source term. The dynamic pressure gradient is treated fully explicit. An initial approximation for the new density field $\rho^0 \approx \rho^{n+1}$ is obtained by explicitly discretizing the continuity Eq. (1a) in time:

$$\rho^0 = \rho^n - \Delta t \frac{\partial \dot{m}_i^n}{\partial x_i}. \tag{7}$$

The mass fluxes $\dot{m}_i^0 = \dot{m}_i^n$ are initialized from the previous time step. Subsequently, a specified number of N_{it} sub-iterations are performed to compute the solution of the entire transport equation system at the new time level t_{n+1}. Starting with $m = 0$, the thermochemical transport equations are solved in a fully coupled manner for the field variables h^{m+1} and Y_s^{m+1}:

$$\left(\frac{\rho^m}{\Delta t} \right) h^{m+1} + \frac{1}{2} \frac{\partial}{\partial x_i} \left(\dot{m}_i^m h^{m+1} - q_i^{m+1} \right) = RHS_h, \tag{8a}$$

$$\left(\frac{\rho^m}{\Delta t} \right) Y_s^{m+1} + \frac{1}{2} \frac{\partial}{\partial x_i} \left(\dot{m}_i^m Y_s^{m+1} - j_{i,s}^{m+1} \right) - \frac{1}{2} \dot{\omega}_s^{m+1} = RHS_{Y_s}. \tag{8b}$$

The implicit calculation of $\dot{\omega}_s^{m+1}$ is carried out by linearization with its analytical Jacobian $\partial \dot{\omega}_s / \partial \Phi_r$

$$\dot{\omega}_s^{m+1} \approx \dot{\omega}_s^n + \left. \frac{\partial \dot{\omega}_s}{\partial \Phi_r} \right|_{t=t_n} \left(\Phi_r^{m+1} - \Phi_r^n \right), \tag{9}$$

with the thermochemical state vector $\mathbf{\Phi} = [h, Y_1, \dots, Y_{N_s-1}]^{\mathrm{T}}$. The implicit diffusive fluxes are calculated by

$$q_i^{m+1} = -\left(\frac{\lambda^n}{c_p^n} \right) \frac{\partial h^{m+1}}{\partial x_i} \qquad \text{and} \qquad j_{i,s}^{m+1} = -\left(\rho^n D_s^n \right) \frac{\partial Y_s^{m+1}}{\partial x_i}. \tag{10}$$

The updated states h^{m+1} and Y_s^{m+1} are used to compute the temperature T^{m+1} and density ρ^{m+1} from the caloric and thermal equation of state

$$T^{m+1} \leftarrow \left(h^{m+1} = \sum_{s=1}^{N_s} h_s(T^{m+1}) Y_s^{m+1} \right) \qquad \text{and} \qquad \rho^{m+1} = \frac{p_0 M^{m+1}}{R_u T^{m+1}}. \tag{11}$$

The mixture's molar mass M^{m+1} is calculated as $M^{m+1} = 1/(\sum_{s=1}^{N_s} Y_s^{m+1}/M_s)$ and the temperature T^{m+1} is determined as a root of the NASA polynomials [40] using a Newton-Raphson method.

Next, the momentum Eq. (1b) are solved using the updated density and the dynamic pressure gradient from the previous time step $\partial p^n / \partial x_i$:

$$\left(\frac{\rho^{m+1}}{\Delta t} \right) u_i^* + \frac{1}{2} \frac{\partial}{\partial x_j} \left(\dot{m}_j^m u_i^* - \tau_{ij}^* \right) = RHS_{u_i}. \tag{12}$$

The resulting velocity field u_i^* does not satisfy the conservation of mass at the new time level t_{n+1} and hence requires correction using a pseudo-pressure field $\delta p = p^{n+1} - p^n$

$$\rho^{n+1} u_i^{n+1} = \rho^{n+1} u_i^* - \Delta t \frac{\partial \delta p}{\partial x_i}. \tag{13}$$

The pseudo-pressure δp is defined such that, upon convergence ($\rho^{m+1} \approx \rho^{n+1}$ and $\dot{m}^m \approx \dot{m}^{n+1}$), substituting Eq. (12) into Eq. (13) results in a discretized momentum equation of the form:

$$\frac{\rho^{n+1} u_i^{n+1} - \rho^n u^n}{\Delta t} + \frac{1}{2}\frac{\partial}{\partial x_j}\left(\dot{m}_j^{n+1} u_i^* - \tau_{ij}^*\right) + \frac{1}{2}\frac{\partial}{\partial x_j}\left(\dot{m}_j^n u_i^n - \tau_{ij}^n\right) = -\frac{\partial p^{n+1}}{\partial x_i}. \tag{14}$$

Eq. (14) introduces a splitting error due to the flux terms u_i^* and τ_{ij}^*, accompanied by a temporal error $\mathcal{O}(\Delta t^2)$. It remains to determine the pseudo-pressure δp. This is achieved by taking the divergence of Eq. (13), resulting in the following Poisson equation for δp:

$$\frac{\partial}{\partial x_i}\left(\frac{\partial \delta p}{\partial x_i}\right) = \frac{1}{\Delta t}\left[\frac{\partial \dot{m}_i^*}{\partial x_i} - \frac{\partial}{\partial x_i}\left(\rho^{n+1} u_i^{n+1}\right)\right], \tag{15}$$

where the mass fluxes $\dot{m}_i^* = \rho^{m+1} u_i^*$ are used to approximate $\partial(\rho^{n+1} u_i^*)/\partial x_i$. Taking into account the continuity Eq. (1a), the term $\partial(\rho^{n+1} u_i^{n+1})/\partial x_i$ is substituted by an approximate temporal derivative of ρ, leading to:

$$\frac{\partial}{\partial x_i}\left(\rho^{n+1} u_i^{n+1}\right) = -\left.\frac{\partial \rho}{\partial t}\right|_{t=t_{n+1}} = -\frac{1}{\Delta t}\left(\frac{3}{2}\rho^{m+1} - 2\rho^n + \frac{1}{2}\rho^{n-1}\right) + \mathcal{O}\left(\Delta t^2\right). \tag{16}$$

This substitution is commonly applied in variable density projection methods, but it is also recognized as a potential source of instability, particularly in cases involving high-density gradients [19,37]. The pressure correction equation is solved during each sub-iteration. Subsequently, the mass fluxes $\dot{m}_i^{m+1}$ are updated according to the Eq. (13) through

$$\dot{m}_i^{m+1} = \dot{m}_i^* - \Delta t \frac{\partial \delta p}{\partial x_i}. \tag{17}$$

Finally, after performing N_{it} sub-iterations, the intermediate velocity field u_i^* and the pressure p^n are corrected using the current pseudo-pressure field δp according to

$$u_i^{n+1} = u_i^* - \frac{\Delta t}{\rho^{m+1}}\frac{\partial \delta p}{\partial x_i} \qquad \text{and} \qquad p^{n+1} = p^n + \delta p. \tag{18}$$

2.3. Spatial discretization

The spatial discretization is carried out with the vertex-centered, k-exact multiple-correction method, which is based on the finite volume method. The approach is illustrated below using a model transport equation of a field variable ϕ

$$\frac{\partial}{\partial t}(\rho\phi) + \frac{\partial}{\partial x_i}\left(\rho u_i \phi\right) - \frac{\partial}{\partial x_i}\left(\rho D \frac{\partial \phi}{\partial x_i}\right) = 0, \tag{19}$$

which describes the transport of ϕ in a flow field with density ρ, velocity $\mathbf{u}$ and diffusivity D. The equation is to be solved in a computational domain Ω, which is discretized by a set of non-overlapping median-dual elements [46]. These are constructed from an underlying tesselation of tetrahedrals, hexahedrals, pyramids and prisms in three dimensions or triangles and quadrilaterals in two dimensions. An exemplary median-dual representation of a two dimensional grid is given in Fig. 1, where two adjacent elements Ω_α and Ω_β share a common face $A_{\alpha\beta}$. All adjacent elements to Ω_α are referred to as its first neighborhood, which is denoted by the set $\{\beta_\alpha^{(1)}\}$.

Central to the finite-volume approach is the volume-average $\overline{\phi}_\alpha$ of the considered field variable over Ω_α

$$\overline{\phi}_\alpha = \frac{1}{|\Omega_\alpha|}\iiint_{\Omega_\alpha} \phi(\mathbf{x})\,\mathrm{d}V. \tag{20}$$

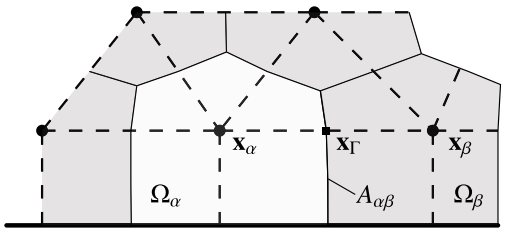

Fig. 1. Median-dual grid in 2D, indicated in solid lines. The corresponding primary grid is drawn in dashed lines. The simulation variables are stored at the location of primary grid nodes, e.g. $\mathbf{x}_\alpha$ or $\mathbf{x}_\beta$.

Applying the volume-averaging operator on Eq. (19) leads to a set of equations where the unknown volume-averages $\overline{\phi}_\alpha$ act as degrees of freedom

$$\frac{\partial}{\partial t}\overline{(\rho\phi)}_\alpha + \frac{1}{|\Omega_\alpha|}\sum_{\beta\in\{\beta_\alpha^{(1)}\}}\left[F_C^{(\alpha\beta)} + F_D^{(\alpha\beta)}\right] = 0. \tag{21}$$

Here, the convective and diffusive fluxes are defined by

$$F_C^{(\alpha\beta)} := \iint_{A_{\alpha\beta}} \left(\rho u_i \phi\right) n_i \,\mathrm{d}A \qquad \text{and} \qquad F_D^{(\alpha\beta)} := \iint_{A_{\alpha\beta}} \left(\rho D \frac{\partial \phi}{\partial x_i}\right) n_i \,\mathrm{d}A, \tag{22}$$

with n_i denoting the unit normal vector.

2.3.1. The k-exact reconstruction approach

To close the system of equations, we aim to approximate the fluxes in terms of $\overline{\phi}_\alpha$ and proceed to a new time step. This is achieved using the k-exact reconstruction approach, where Taylor polynomials $\phi^{(k+1)}(\mathbf{x};\mathbf{x}_\alpha)$ of degree k are used to approximate the solution in the vicinity of an element Ω_α:

$$\phi^{(k+1)}(\mathbf{x};\mathbf{x}_\alpha) = \phi\Big|_{\mathbf{x}_\alpha}^{(k+1)} + \frac{\partial\phi}{\partial x_{i_1}}\Big|_{\mathbf{x}_\alpha}^{(k)}\left(x_{i_1} - x_{i_1,\alpha}\right) + \ldots + \frac{1}{k!}\frac{\partial^k\phi}{\partial x_{i_1}\ldots\partial x_{i_k}}\Big|_{\mathbf{x}_\alpha}^{(1)}\left(x_{i_1} - x_{i_1,\alpha}\right)\ldots\left(x_{i_k} - x_{i_k,\alpha}\right). \tag{23}$$

These polynomials are expanded around the nodal positions $\mathbf{x}_\alpha$, which define the median-dual elements Ω_α. In Eq. (23), a special notation distinguishes polynomial coefficients from true point values of the solution. Here, $\phi|_{\mathbf{x}_\alpha}^{(k+1)}$ represents an approximated point value $\phi(\mathbf{x}_\alpha)$ with accuracy $\mathcal{O}(h^{k+1})$, where h denotes the local grid scale. Similarly, the n^{th} derivative term refers to an approximation of the true point derivative at $\mathbf{x}_\alpha$ with accuracy $\mathcal{O}(h^{k-n+1})$.

The classical k-exact method determines these unknown polynomial coefficients by requiring that the volume-averaged polynomial in Eq. (23) matches the volume-averaged solution of neighboring elements to the corresponding accuracy. This leads to a least-squares system that is solved for each element Ω_α [47–49]. While robust, this approach introduces complex data dependencies: cell-averaged solution values from potentially multiple layers of neighboring elements are needed across decomposed domain boundaries in parallel computations. Consequently, additional layers of ghost elements must be communicated between processors, increasing implementation effort and potentially reducing parallel efficiency. The k-exact multiple-correction approach [2,4] alleviates these issues by successively estimating the polynomial coefficients from correction steps based on Green-Gauss gradients.

The latter approximate the gradient of ϕ at $\mathbf{x}_\alpha$ using volume-averages of all direct neighbors of Ω_α

$$\frac{\partial\phi}{\partial x_i}\Big|_{\mathbf{x}_\alpha}^{(0)} = \frac{1}{|\Omega_\alpha|}\sum_{\beta\in\{\beta_\alpha^{(1)}\}}\frac{1}{2}\left(\overline{\phi}_\alpha + \overline{\phi}_\beta\right)S_i^{(\alpha\beta)}, \tag{24}$$

where $S_i^{(\alpha\beta)}$ denotes the surface normal vector between two adjacent elements Ω_α and Ω_β. On general unstructured grids, these gradients lack sufficient accuracy for direct use in Eq. (23). To overcome this, the multiple-correction approach applies grid-specific correction matrices $\mathbf{G}_\alpha^{(k)}$ to improve accuracy. For a 1-exact gradient, this correction takes the form:

$$\frac{\partial\phi}{\partial x_i}\Big|_{\mathbf{x}_\alpha}^{(1)} = G_{\alpha,ij}^{(1)}\,\frac{\partial\phi}{\partial x_j}\Big|_{\mathbf{x}_\alpha}^{(0)}. \tag{25}$$

This corrected gradient is then used to compute higher derivatives recursively - for example, estimating the Hessian matrix of ϕ:

$$\frac{\partial^2\phi}{\partial x_i\partial x_j}\Big|_{\mathbf{x}_\alpha}^{(0)} = \frac{1}{|\Omega_\alpha|}\sum_{\beta\in\{\beta_\alpha^{(1)}\}}\frac{1}{2}\left(\frac{\partial\phi}{\partial x_i}\Big|_{\mathbf{x}_\alpha}^{(1)} + \frac{\partial\phi}{\partial x_i}\Big|_{\mathbf{x}_\beta}^{(1)}\right)S_j^{(\alpha\beta)}, \tag{26}$$

followed by further correction steps involving both the Hessian matrix and the gradient:

$$\frac{\partial^2\phi}{\partial x_i\partial x_j}\Big|_{\mathbf{x}_\alpha}^{(1)} = H_{\alpha,ijkl}^{(1)}\,\frac{\partial^2\phi}{\partial x_k\partial x_l}\Big|_{\mathbf{x}_\alpha}^{(0)} \qquad \rightarrow \qquad \frac{\partial\phi}{\partial x_i}\Big|_{\mathbf{x}_\alpha}^{(2)} = \frac{\partial\phi}{\partial x_i}\Big|_{\mathbf{x}_\alpha}^{(1)} - G_{\alpha,ijk}^{(2)}\,\frac{\partial^2\phi}{\partial x_j\partial x_k}\Big|_{\mathbf{x}_\alpha}^{(1)}, \tag{27}$$

where $\mathbf{H}_\alpha^{(1)}$ and $\mathbf{G}_\alpha^{(2)}$ denote further correction matrices.

A key advantage of this approach lies in its data exchange requirements. Unlike the least-squares method, which involves non-local stencils spanning multiple layers of elements, the multiple-correction scheme requires only derivatives from direct neighbors. As a result, the MPI communication across decomposed domain boundaries is limited to first-layer ghost elements - no additional transfer of extended stencil data is needed. This design considerably simplifies integration into existing solvers and enhances parallel scalability, particularly for large-scale simulations on unstructured grids.

The correction matrices $\mathbf{G}_\alpha^{(1)}, \mathbf{G}_\alpha^{(2)}, \mathbf{H}_\alpha^{(1)}$ represent tensors of different ranks, whose calculation for cell-centered grids can be found in the work of Pont et al. [2] and for median-dual grids in our previous work [4]. There, it is also shown how the costly tensor product in Eq. (27) can be turned to a matrix-vector product by utilizing the symmetry properties of the Hessian. The calculation of

all correction matrices depends primarily on grid-dependent metrics, which are referred to as geometric volume moments. These are generally defined by

$$\mathcal{M}_{i_1 i_2 \dots i_p,\alpha} = \frac{1}{|\Omega_\alpha|} \iiint_{\Omega_\alpha} \left(x_{i_1} - x_{i_1,\alpha}\right)\left(x_{i_2} - x_{i_2,\alpha}\right) \dots \left(x_{i_p} - x_{i_p,\alpha}\right) \mathrm{d}V, \tag{28}$$

where $\mathcal{M}_{i_1 i_2 \dots i_p,\alpha}$ refers to a moment of rank p. The moment calculation for polyhedral elements can be found in the literature [50,51]. The final coefficient to be determined in Eq. (23) is the point value $\phi|_{\mathbf{x}_\alpha}^{(k+1)}$. It is related to the volume-average $\overline{\phi}_\alpha$ by averaging the reconstruction polynomial volumetrically over Ω_α and by taking into account the introduced $\mathcal{M}_{i_1 i_2 \dots i_p,\alpha}$, as well as the corrected derivatives:

$$\phi\Big|_{\mathbf{x}_\alpha}^{(k+1)} = \overline{\phi}_\alpha - \frac{\partial \phi}{\partial x_{i_1}}\bigg|_{\mathbf{x}_\alpha}^{(k)} \mathcal{M}_{i_1,\alpha} - \dots - \frac{1}{k!}\frac{\partial^k \phi}{\partial x_{i_1} \dots \partial x_{i_k}}\bigg|_{\mathbf{x}_\alpha}^{(1)} \mathcal{M}_{i_1 \dots i_k,\alpha} + \mathcal{O}\left(h^{k+1}\right). \tag{29}$$

Finally, Eq. (21) contains volume-averaged conservative variables $\overline{(\rho\phi)}_\alpha$ which must be transformed into their corresponding primitive counterparts $\overline{\rho}_\alpha$ and $\overline{\phi}_\alpha$. We can derive a relation by approximating ρ and ϕ analogously to Eq. (23) by Taylor polynomials, which are then to be offset against each other and volume-averaged over Ω_α. By comparing the mean values of these separate Taylor polynomials, we can extract the deviation between $\overline{(\rho\phi)}_\alpha$ and $\overline{\rho}_\alpha\overline{\phi}_\alpha$ to

$$\overline{(\rho\phi)}_\alpha = \overline{\rho}_\alpha\overline{\phi}_\alpha - \frac{\partial \rho}{\partial x_i}\bigg|_{\mathbf{x}_\alpha}^{(k)} \frac{\partial \phi}{\partial x_j}\bigg|_{\mathbf{x}_\alpha}^{(k)} \left(\mathcal{M}_{i,\alpha}\mathcal{M}_{j,\alpha} - \mathcal{M}_{ij,\alpha}\right) + \mathcal{O}\left(h^3\right). \tag{30}$$

This shows that a second-order spatial error arises when two conservatively averaged variables $\overline{(\rho\phi)}_\alpha$ are replaced with the product of their primitive means $\overline{\rho}_\alpha\overline{\phi}_\alpha$.

2.3.2. Limitation

In combustion simulations, a high-order reconstruction might induce parasitic errors due to the steep gradients near the flame front, which can be attributed to the Gibbs phenomenon [1,52]. To circumvent this, we apply the gradient limiting approach by Barth and Jespersen [46] to limit the reconstruction of thermochemical variables, such as the enthalpy h, the density ρ and the species mass fractions Y_s. The reconstruction polynomial of a field variable ϕ is extended by a limiter variable ψ_α

$$\phi^{(k+1)}(\mathbf{x};\mathbf{x}_\alpha) = \overline{\phi}_\alpha + \psi_\alpha\, \Delta\phi_\alpha^{(k+1)}(\mathbf{x}), \tag{31}$$

where the term $\Delta\phi_\alpha^{(k+1)}(\mathbf{x})$ contains the derivatives and the contribution of the geometric volume moments that result from the conversion from point values to volume averages (the right hand side of Eq. (29) excluding $\overline{\phi}_\alpha$). For $k = 2$, these termse are given by

$$\Delta\phi_\alpha^{(3)}(\mathbf{x}) = \frac{\partial \phi}{\partial x_i}\bigg|_{\mathbf{x}_\alpha}^{(2)} \left(x_i - x_{i,\alpha} - \mathcal{M}_{i,\alpha}\right) + \frac{1}{2}\frac{\partial^2 \phi}{\partial x_i \partial x_j}\bigg|_{\mathbf{x}_\alpha}^{(1)} \left[\left(x_i - x_{i,\alpha}\right)\left(x_j - x_{j,\alpha}\right) - \mathcal{M}_{ij,\alpha}\right]. \tag{32}$$

The limiter variable ψ_α is calculated using [46]

$$\psi_\alpha = \min_{\Gamma \in \{\Gamma_\alpha\}} \begin{cases} \min(1, y) & \text{for} \quad \Delta\phi_\alpha^{(k+1)}(\mathbf{x}_\Gamma) \neq 0, \\ 1 & \text{for} \quad \Delta\phi_\alpha^{(k+1)}(\mathbf{x}_\Gamma) = 0, \end{cases} \tag{33}$$

where the set $\{\Gamma_\alpha\}$ comprises the points $\mathbf{x}_\Gamma$ at which the fluxes of an element Ω_α are calculated. The quantity y in function $\min(1, y)$ is calculated at these points via [46,53]

$$y = \max\left[\frac{\left(\overline{\phi}_{\min} - \epsilon_\alpha\right) - \overline{\phi}_\alpha}{\Delta\phi_\alpha^{(k+1)}(\mathbf{x}_\Gamma)}, \quad \frac{\left(\overline{\phi}_{\max} + \epsilon_\alpha\right) - \overline{\phi}_\alpha}{\Delta\phi_\alpha^{(k+1)}(\mathbf{x}_\Gamma)}\right]. \tag{34}$$

The $\min(1, y)$ function in Eq. (33) ensures that the reconstruction polynomial stays between $\left(\overline{\phi}_{\min} - \epsilon_\alpha\right)$ and $\left(\overline{\phi}_{\max} + \epsilon_\alpha\right)$ when limited with ψ_α [46,53]. $\overline{\phi}_{\min}$ and $\overline{\phi}_{\max}$ indicate the smallest negative and largest positive volumetric averages in the first neighborhood $\{\beta_\alpha^{(1)}\}$, respectively. The value ϵ_α represents an element specific threshold that artificially extends the interval $\left[\overline{\phi}_{\min}, \overline{\phi}_{\max}\right]$. It represents a modification to the original limiting approach according to Moe et al. [54] and is used to prevent an unwanted activation of the limiter in smooth regions. Similar approaches for deactivating the limitation were used in the work of Michalak and Ollivier-Gooch [55], Nishikawa [53] and Venkatakrishnan [56] by adapting the $\min(1, y)$ function. In the work of Moe et al. it was shown that ϵ_α must scale with the factor $\mathcal{O}(h^r)$ and $r \leq 2$, in order to obtain a higher spatial error order near smooth extrema of the solution. In this work, it is calculated by $\epsilon_\alpha = K\,\nabla\phi\,\tilde{h}$, where $K = 1/2$ denotes a constant and $\nabla\phi$ is a global gradient based upon the extrema of ϕ from the entire domain Ω divided by the maximum length scale of the domain L. The value $\tilde{h}$ denotes a local length scale which is calculated by $\tilde{h} = \sqrt{|\Omega_\alpha|/L}$, to scale with $\mathcal{O}(h^{3/2})$. ϵ_α is updated in each time step for each field variable, which, in particular, helps to ensure that the limiter remains switched off for all species equally in smooth regions - especially for the minor species with very small scales. A similar approach has been utilized in the work of Wang [57]. In the work of Tsoutsanis [58] it was shown that

the use of the first neighborhood to determine the values $\overline{\phi}_{\min}$ and $\overline{\phi}_{\max}$ in the Barth-Jespersen method for $k > 1$ can be associated with a reduced order of accuracy. This is due to activation of the limiter variable when the grid quality is poor. However, Tsoutsanis showed that this error can be reduced by searching for the extremes $\overline{\phi}_{\min}$ and $\overline{\phi}_{\max}$ in the entire neighborhood $\{\beta_\alpha^{(k)}\}$, which is used for the k-exact reconstruction. This improvement could also be determined in numerical experiments for the vertex-centered k-exact multiple-correction method and is used for the 2-exact method in the further course of this work.

2.3.3. Approximation of fluxes

Following the reconstruction of the solution, we utilize $\phi^{(k+1)}(\mathbf{x};\mathbf{x}_\alpha)$ to approximate the surface integrals of transport Eq. (19) to close the system of equations. The approximation of the numerical fluxes $F_C^{(\alpha\beta)}$ and $F_D^{(\alpha\beta)}$ is realized with a single-point integration, which is based on a Taylor series expansion around a point $\mathbf{x}_\Gamma = (\mathbf{x}_\alpha + \mathbf{x}_\beta)/2$ located on the surface $A_{\alpha\beta}$:

$$\iint_{A_{\alpha\beta}} f_i\, n_i \,\mathrm{d}A = f_i\Big|_{\mathbf{x}_\Gamma} S_i^{(\alpha\beta)} + \frac{\partial f_i}{\partial x_{j_1}}\bigg|_{\mathbf{x}_\Gamma} S_{i,j_1}^{(\alpha\beta,\Gamma)} + \ldots + \frac{1}{k!}\,\frac{\partial^k f_i}{\partial x_{j_1}\ldots\partial x_{j_k}}\bigg|_{\mathbf{x}_\Gamma} S_{i,j_1\ldots j_k}^{(\alpha\beta,\Gamma)} + \mathcal{O}\big(h^{k+1}\big). \tag{35}$$

This expression allows us to integrate any flux function f_i by means of the reconstructed point value $\phi|_{\mathbf{x}_\Gamma}$ and its derivatives at $\mathbf{x}_\Gamma$, as long as these values maintain appropriate orders of accuracies. The integration is based on rank p geometric surface moments, which ensure a proper integration of the surface-integral in a single point, regardless of the shape of the surface $A_{\alpha\beta}$. These moments are generally defined as

$$S_{i,j_1 j_2\ldots j_p}^{(\alpha\beta,\Gamma)} = \iint_{A_{\alpha\beta}} n_i \Big(x_{j_1} - x_{j_1,\Gamma}\Big)\Big(x_{j_2} - x_{j_2,\Gamma}\Big)\ldots\Big(x_{j_p} - x_{j_p,\Gamma}\Big)\,\mathrm{d}A, \tag{36}$$

where the subscripts i and j_p are separated by a comma, to highlight that i indicates the face normal direction and j_p the spatial direction of the terms $\left(x_{j_p} - x_{j_p,\Gamma}\right)$. The superscripts $(\alpha\beta,\Gamma)$ indicate the elements Ω_α and Ω_β adjacent to the face, as well as the point $\mathbf{x}_\Gamma$ where the Taylor series expansion is located. The rank zero surface moment $S_i^{(\alpha\beta)}$ does not include the superscript Γ since it only refers to the joint normal of the face $A_{\alpha\beta}$ and is thus independent of $\mathbf{x}_\Gamma$.

2.3.4. Convective fluxes

To approximate the convective fluxes, we substitute the flux function $f_i = (\rho u_i \phi)$ by two separate reconstruction polynomials for (ρu_i) and ϕ. The resulting product is evaluated at point $\mathbf{x}_\Gamma$. The derivatives of f_i are approximated in a similar fashion. For $k = 2$, we introduce the integrated mass flux $\dot{m}^{(\alpha\beta,\Gamma)}$ and its higher order tensors $\dot{m}_i^{(\alpha\beta,\Gamma)}$, $\dot{m}_{ij}^{(\alpha\beta,\Gamma)}$

$$\dot{m}^{(\alpha\beta,\Gamma)} = (\rho u_i)\Big|_{\mathbf{x}_\Gamma}^{(3)} S_i^{(\alpha\beta)} + \frac{\partial}{\partial x_j}(\rho u_i)\bigg|_{\mathbf{x}_\Gamma}^{(2)} S_{i,j}^{(\alpha\beta,\Gamma)} + \frac{1}{2}\,\frac{\partial^2}{\partial x_j \partial x_k}(\rho u_i)\bigg|_{\mathbf{x}_\Gamma}^{(1)} S_{i,jk}^{(\alpha\beta,\Gamma)}, \tag{37a}$$

$$\dot{m}_i^{(\alpha\beta,\Gamma)} = (\rho u_j)\Big|_{\mathbf{x}_\Gamma}^{(3)} S_{j,i}^{(\alpha\beta,\Gamma)} + \frac{\partial}{\partial x_k}(\rho u_j)\bigg|_{\mathbf{x}_\Gamma}^{(2)} S_{j,ki}^{(\alpha\beta,\Gamma)}, \tag{37b}$$

$$\dot{m}_{ij}^{(\alpha\beta,\Gamma)} = (\rho u_k)\Big|_{\mathbf{x}_\Gamma}^{(3)} S_{k,ij}^{(\alpha\beta,\Gamma)}. \tag{37c}$$

Upon application of the product rule to the product of the reconstructed functions for (ρu_i) and ϕ, the convective flux integral can be reformulated into

$$F_C^{(\alpha\beta)} = \dot{m}^{(\alpha\beta,\Gamma)}\,\phi\Big|_{\mathbf{x}_\Gamma}^{(3)} + \dot{m}_i^{(\alpha\beta,\Gamma)}\,\frac{\partial\phi}{\partial x_i}\bigg|_{\mathbf{x}_\Gamma}^{(2)} + \frac{1}{2}\,\dot{m}_{ij}^{(\alpha\beta,\Gamma)}\,\frac{\partial^2\phi}{\partial x_i \partial x_j}\bigg|_{\mathbf{x}_\Gamma}^{(1)} + |A_{\alpha\beta}|\,\mathcal{O}\big(h^3\big). \tag{38}$$

Due to the definition of the geometric surface moments, all terms scale with $\left|A_{\alpha\beta}\right|$. The mass flux tensors in Eqs. (37b) and (37c) scale with $\mathcal{O}(h^2)$ and $\mathcal{O}(h)$, respectively. Hence, an overall spatial error of $\mathcal{O}(h^3)$ can be accomplished for the flux approximation using Eq. (38) and a 2-exact reconstruction. In the case of a $k = 1$, the second derivatives are omitted and an error $\mathcal{O}(h^2)$ is achieved. The terms (ρu_i) at location $\mathbf{x}_\Gamma$ are calculated from the reconstructed values of ρ and u_i using the following relations

$$(\rho u_i)\Big|_{\mathbf{x}_\Gamma}^{(3)} = \rho\Big|_{\mathbf{x}_\Gamma}^{(3)} u_i\Big|_{\mathbf{x}_\Gamma}^{(3)}, \tag{39a}$$

$$\frac{\partial(\rho u_i)}{\partial x_j}\bigg|_{\mathbf{x}_\Gamma}^{(2)} = \rho\Big|_{\mathbf{x}_\Gamma}^{(3)} \frac{\partial u_i}{\partial x_j}\bigg|_{\mathbf{x}_\Gamma}^{(2)} + u_i\Big|_{\mathbf{x}_\Gamma}^{(3)} \frac{\partial\rho}{\partial x_j}\bigg|_{\mathbf{x}_\Gamma}^{(2)}, \tag{39b}$$

$$\frac{\partial^2(\rho u_i)}{\partial x_j \partial x_k}\bigg|_{\mathbf{x}_\Gamma}^{(1)} = \rho\Big|_{\mathbf{x}_\Gamma}^{(3)} \frac{\partial^2 u_i}{\partial x_j \partial x_k}\bigg|_{\mathbf{x}_\Gamma}^{(1)} + u_i\Big|_{\mathbf{x}_\Gamma}^{(3)} \frac{\partial^2\rho}{\partial x_j \partial x_k}\bigg|_{\mathbf{x}_\Gamma}^{(1)} + \frac{\partial\rho}{\partial x_j}\bigg|_{\mathbf{x}_\Gamma}^{(2)} \frac{\partial u_i}{\partial x_k}\bigg|_{\mathbf{x}_\Gamma}^{(2)} + \frac{\partial\rho}{\partial x_k}\bigg|_{\mathbf{x}_\Gamma}^{(2)} \frac{\partial u_i}{\partial x_j}\bigg|_{\mathbf{x}_\Gamma}^{(2)}. \tag{39c}$$

To calculate the field variables ρ, u_i and ϕ at location $\mathbf{x}_\Gamma$, we utilize the respective reconstruction functions from the two adjacent elements Ω_α and Ω_β, combined with an adaptive numerical dissipation control. The latter is based upon an upwind bias value $\theta \in [0, 1]$, which enables us to control the amount of numerical dissipation introduced by the scheme

$$\phi\Big|_{\mathbf{x}_\Gamma}^{(3)} = \frac{1}{2}\left[\phi^{(3)}(\mathbf{x}_\Gamma;\mathbf{x}_u) + \phi^{(3)}(\mathbf{x}_\Gamma;\mathbf{x}_d)\right] - \frac{\theta}{2}\left[\phi^{(3)}(\mathbf{x}_\Gamma;\mathbf{x}_d) - \phi^{(3)}(\mathbf{x}_\Gamma;\mathbf{x}_u)\right]. \tag{40}$$

Index u denotes the element upstream of $A_{\alpha\beta}$ and d the element downstream. This formulation is similar to generalized Lax-Friedrichs flux [59] and has, for example, also been used in the work of Mary and Sagaut [60] or Pont et al. [2]. The former term represents a purely central approximation of $\phi|^{(3)}_{\mathbf{x}_\Gamma}$, whereas the trailing term controls the degree to which the solution is favored from the upstream side, hence, introducing numerical dissipation without affecting the formal order of accuracy. Derivatives at the interface location $\mathbf{x}_\Gamma$ are reconstructed in a similar fashion via

$$\left.\frac{\partial \phi}{\partial x_i}\right|^{(2)}_{\mathbf{x}_\Gamma} = \frac{1}{2}\left[\frac{\partial}{\partial x_i}\phi^{(3)}(\mathbf{x}_\Gamma;\mathbf{x}_u) + \frac{\partial}{\partial x_i}\phi^{(3)}(\mathbf{x}_\Gamma;\mathbf{x}_d)\right] - \frac{\theta}{2}\left[\frac{\partial}{\partial x_i}\phi^{(3)}(\mathbf{x}_\Gamma;\mathbf{x}_d) - \frac{\partial}{\partial x_i}\phi^{(3)}(\mathbf{x}_\Gamma;\mathbf{x}_u)\right], \tag{41}$$

$$\left.\frac{\partial^2 \phi}{\partial x_i \partial x_j}\right|^{(1)}_{\mathbf{x}_\Gamma} = \frac{1}{2}\left[\frac{\partial^2}{\partial x_i \partial x_j}\phi^{(3)}(\mathbf{x}_\Gamma;\mathbf{x}_u) + \frac{\partial^2}{\partial x_i \partial x_j}\phi^{(3)}(\mathbf{x}_\Gamma;\mathbf{x}_d)\right] - \frac{\theta}{2}\left[\frac{\partial^2}{\partial x_i \partial x_j}\phi^{(3)}(\mathbf{x}_\Gamma;\mathbf{x}_d) - \frac{\partial^2}{\partial x_i \partial x_j}\phi^{(3)}(\mathbf{x}_\Gamma;\mathbf{x}_u)\right]. \tag{42}$$

Taking into account the method described for limiting the reconstruction polynomial, the convective flux can be represented by the following two terms

$$F_C^{(\alpha\beta)} = F_{C,LO}^{(\alpha\beta)} + F_{C,HO}^{(\alpha\beta)} + |A_{\alpha\beta}|\,\mathcal{O}\left(h^3\right), \tag{43}$$

where former term $F_{C,LO}^{(\alpha\beta)}$ contains all contributions of a 0-exact reconstruction:

$$F_{C,LO}^{(\alpha\beta)} = \frac{1}{2}\dot{m}^{(\alpha\beta,\Gamma)}\left(\overline{\phi}_u + \overline{\phi}_d\right) - \frac{\theta}{2}\dot{m}^{(\alpha\beta,\Gamma)}\left(\overline{\phi}_d - \overline{\phi}_u\right). \tag{44}$$

For $\theta = 1$ this term changes to a pure upwind method, which is necessary to prevent the emergence of new extrema in the sense of Godunov's theorem. The term $F_{C,HO}^{(\alpha\beta)}$ accounts for the high-order reconstruction with $k > 0$ and is defined by

$$\begin{aligned} F_{C,HO}^{(\alpha\beta)} = {} & \dot{m}^{(\alpha\beta,\Gamma)}\left[\psi_u\left(\frac{1+\theta}{2}\right)\Delta\phi_u^{(3)}(\mathbf{x}_\Gamma) + \psi_d\left(\frac{1-\theta}{2}\right)\Delta\phi_d^{(3)}(\mathbf{x}_\Gamma)\right] \\ & + \dot{m}_i^{(\alpha\beta,\Gamma)}\left[\psi_u\left(\frac{1+\theta}{2}\right)\frac{\partial}{\partial x_i}\phi^{(2)}(\mathbf{x}_\Gamma;\mathbf{x}_u) + \psi_d\left(\frac{1-\theta}{2}\right)\frac{\partial}{\partial x_i}\phi^{(2)}(\mathbf{x}_\Gamma;\mathbf{x}_d)\right] \\ & + \frac{1}{2}\dot{m}_{ij}^{(\alpha\beta,\Gamma)}\left[\psi_u\left(\frac{1+\theta}{2}\right)\frac{\partial^2}{\partial x_i \partial x_j}\phi^{(1)}(\mathbf{x}_\Gamma;\mathbf{x}_u) + \psi_d\left(\frac{1-\theta}{2}\right)\frac{\partial^2}{\partial x_i \partial x_j}\phi^{(1)}(\mathbf{x}_\Gamma;\mathbf{x}_d)\right]. \end{aligned} \tag{45}$$

It can be deactivated via the limiter variables ψ_u and ψ_d, which are calculated using Eq. (31). This separation of the convective flux in two terms is also taken into account when solving the entire system of equations. Since $F_{C,LO}^{(\alpha\beta)}$ involves only volume averages from face-neighboring elements, an implicit treatment of this term leads to a compact element molecule in the system matrix. In contrast, the term $F_{C,HO}^{(\alpha\beta)}$ contains derivatives of ϕ and thus indirectly the information of elements at a greater distance. Hence, an implicit calculation would cause a large element molecule in the system matrix and require a constant update of all derivatives within sub-iterations of the solution algorithm. To save computing time, a deferred correction strategy is utilized [61,62] where $F_{C,LO}^{(\alpha\beta)}$ is treated implicitly and $F_{C,HO}^{(\alpha\beta)}$ explicitly.

2.3.5. Upwind bias

The calculation of the upwind bias θ for incompressible flows has been discussed in a previous work [5], where an advection-diffusion model equation was discretized using the proposed k-exact method, followed by a Von Neumann stability analysis. This analysis allowed the derivation of a stability criterion for the method, which in turn was used to determine θ. As result, θ could be calculated at each surface of the computational grid using a stability equation that depends on a local Courant-Friedrichs-Lewy (CFL) number σ, a local grid Reynolds number Re_h and the limiter variables ψ_u and ψ_d of the upstream and downstream elements, respectively. The stability equation is expressed as

$$\theta_{\max}(\sigma, \mathrm{Re}_h, \psi_u, \psi_d) = \max_{\omega_j}\left[\frac{-B(\omega_j) - \sqrt{B^2(\omega_j) - 4A(\omega_j)C(\omega_j)}}{2A(\omega_j)}\right], \tag{46}$$

where ω_j is the wavenumber resulting from the Fourier transformation in the Von Neumann analysis. For the precise definitions of coefficients A, B and C, we refer to the previous work [5], where a comprehensive overview is provided. In addition to being influenced by the wavenumber ω_j, these coefficients depend on the parameters σ, Re_h, ψ_u and ψ_d. Eq. (46) allows us to predict the upwind bias θ so that the k-exactly discretized model equation remains stable. This approach minimizes the numerical dissipation introduced by the method, preserving the accuracy of the solution. However, the downside of this equation is that its calculation is computationally expensive and must be performed at every interface between elements of the computational grid. In the previous work, only the limiter states $\psi_u, \psi_d = \{0, 1\}$ were considered, focusing on deactivating the reconstruction in specific regions. To address the computational cost, Eq. (46) was approximated using compact neural network functions that depend solely on the CFL number σ and the grid Reynolds number Re_h. This approach made the calculation of θ negligible in terms of computation time. In this work, we extend this methodology to cover the entire range of limiter variables $\psi_u, \psi_d \in [0, 1]$. This enables the gradient limitation described in Section 2.3.2 to be combined with an adaptive upwind bias calculation, which reduces the introduced amount of numerical dissipation even in limited regions of the domain.

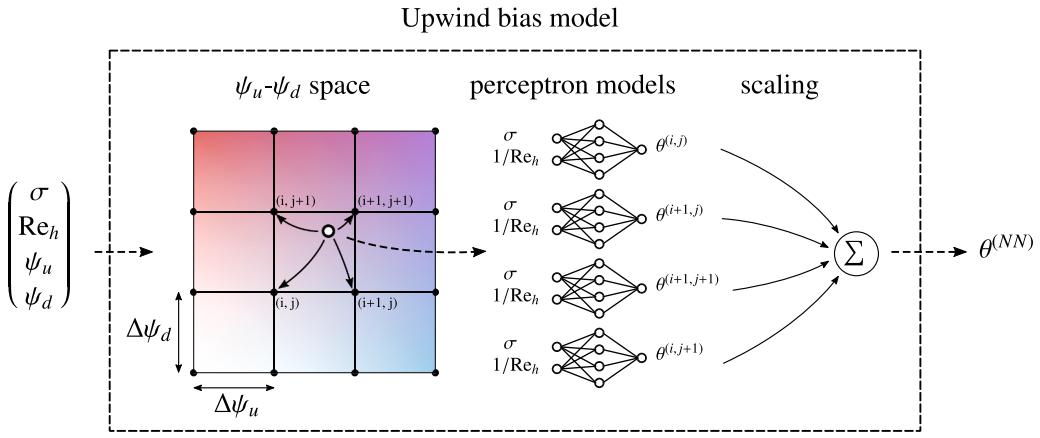

Fig. 2. Calculation of the upwind bias θ.

The parameter space $\psi_u \times \psi_d$ is uniformly discretized into 8×8 grid points, with each grid point associated with a dedicated neural network model that takes the local flow parameters (σ, Re_h) as inputs. The choice of 8×8 points was determinded through a trial-and-error procedure to balance model accuracy and computational efficiency. Selecting a power-of-two discretization further enables efficient identification of neighboring models in the $\psi_u \times \psi_d$ space via binary modulo operations.

The model parameters σ and Re_h are determined based on the corresponding ranges of values from Eq. (46). This segregated approach was chosen over a fully connected neural network with all four input variables for several reasons. First, it allowed us to leverage the existing training infrastructure with minimal modifications, requiring only an adjustment of the training data based on the two limiter values. Second, due to the low dimensionality of the problem, we could employ Levenberg-Marquardt optimization during training, as successfully used in previous work. This was followed by a fine-tuning step using Gradient Descent to prevent the models from underpredicting the upwind bias, which would otherwise violate the stability criterion. Compared to training a fully connected network with all four input variables, this strategy led to significantly improved upwind bias predictions. Furthermore, this approach substantially reduced computational costs, as the smaller networks were much more efficient to execute, and selecting the best-performing network for a given limiter pair could be implemented with high efficiency. For a detailed comprehension on the methodology to determine the structure of the perceptron models and their weights we refer to our previous work [5].

For the flux calculation at a face $A_{\alpha\beta}$, the limiter values (ψ_u, ψ_d) of the adjacent elements are used to locate the four surrounding grid nodes - $(i,j), (i+1,j), (i,j+1), (i+1,j+1)$ - that enclose the input point in the discretized $\psi_u \times \psi_d$-space. These four models are evaluated with the local inputs (σ, Re_h), yielding corresponding upwind bias values $\theta^{(i,j)}$. The final upwind bias $\theta^{(NN)}$ is then computed by bilinear interpolation of these four outputs:

$$\theta^{(NN)} = (1-s)(1-t)\,\theta^{(i,j)} + s(1-t)\,\theta^{(i+1,j)} + st\,\theta^{(i+1,j+1)} + (1-s)t\,\theta^{(i,j+1)}, \tag{47}$$

where the weights $s = (\psi_u/\Delta\psi_u) - i$ and $t = (\psi_d/\Delta\psi_d) - j$ are determined from the relative position of the input point within the local grid cell, and $\Delta\psi_u$, $\Delta\psi_d$ denote the grid increments. This bilinear interpolation approach, using only the four immediate neighbors, is a standard and efficient method for interpolating structured 2D grids and fully captures the local variation without requiring additional nodes. Finally, $\theta^{(NN)}$ is clipped to the value range $[0, 1]$. A schematic overview of this procedure is provided in Fig. 2.

2.3.6. *Diffusive fluxes*

The calculation of the diffusive fluxes is based on a k-exact extension of Mathur and Murthy's scheme [32], which has been presented in our recent publication [6]. There it was also shown, that it can be cast into the well-known α-damping scheme [34]. The following is a brief description of the approach for $k = 2$. Starting point is the flux function $f_i = D\,(\partial\phi/\partial x_i)$, which is inserted Eq. (35)

$$F_D^{(\alpha\beta)} = \rho D \left.\frac{\partial\phi}{\partial x_i}\right|_{\mathbf{x}_\Gamma} S_i^{(\alpha\beta)} + \rho D \left.\frac{\partial^2\phi}{\partial x_i \partial x_j}\right|_{\mathbf{x}_\Gamma} S_{i,j}^{(\alpha\beta,\Gamma)} + |A_{\alpha\beta}|\,\mathcal{O}\big(h^2\big). \tag{48}$$

The method aims to express the gradient $\partial\phi/\partial x_i|_{\mathbf{x}_\Gamma}$ in terms of the volume-averages of the adjacent elements Ω_α and Ω_β, which results in a stronger coupling of the underlying system of equations and a suppression of parasitic errors [32]. It relies on separating the scalar product between the gradient and the surface normal $(\partial\phi/\partial x_i|_{\mathbf{x}_\Gamma}) S_i^{(\alpha\beta)}$ into orthogonal and non-orthogonal parts [63]

$$\left.\frac{\partial\phi}{\partial x_i}\right|_{\mathbf{x}_\Gamma} S_i^{(\alpha\beta)} = \varepsilon^{(\alpha\beta)} \left.\frac{\partial\phi}{\partial x_i}\right|_{\mathbf{x}_\Gamma} \Delta x_i^{(\alpha\beta)} + \varepsilon^{(\alpha\beta)} \left.\frac{\partial\phi}{\partial x_i}\right|_{\mathbf{x}_\Gamma} \Delta\tilde{x}_i^{(\alpha\beta)} \tag{49}$$

with the distance vectors $\Delta x_i^{(\alpha\beta)} := x_{i,\beta} - x_{i,\alpha}$ and $\Delta\tilde{x}_i^{(\alpha\beta)} := S_i^{(\alpha\beta)}/\varepsilon^{(\alpha\beta)} - \Delta x_i^{(\alpha\beta)}$. The scalar $\varepsilon^{(\alpha\beta)}$ places a degree of freedom for the construction of the scheme. For the present work, it is calculated according to the over-relaxed approach [63]:

$$\varepsilon^{(\alpha\beta)} = \frac{S_i^{(\alpha\beta)} S_i^{(\alpha\beta)}}{\Delta x_j^{(\alpha\beta)}\, S_j^{(\alpha\beta)}}, \tag{50}$$

which leads to a stronger weighting of the non-orthogonal part when the surface normal $S_i^{(\alpha\beta)}$ and the distance vector $\Delta x_i{}^{(\alpha\beta)}$ are not aligned [63]. To unify the method with the k-exact approach, the two scalar products in Eq. (49) are expressed by the reconstruction polynomials of the adjacent elements. For $k = 2$, the diffusive flux can be finally expressed by

$$\begin{aligned} F_D^{(\alpha\beta)} = {} & \epsilon^{(\alpha\beta)}\rho_\Gamma D_\Gamma \left(\phi\big|_{\mathbf{x}_\beta}^{(3)} - \phi\big|_{\mathbf{x}_\alpha}^{(3)} \right) + \frac{1}{2}\rho_\Gamma D_\Gamma \left(\frac{\partial\phi}{\partial x_i}\bigg|_{\mathbf{x}_\alpha}^{(2)} + \frac{\partial\phi}{\partial x_i}\bigg|_{\mathbf{x}_\beta}^{(2)} \right) \left(S_i^{(\alpha\beta)} - \epsilon^{(\alpha\beta)}\Delta x_i{}^{(\alpha\beta)} \right) \\ & - \frac{1}{4}\rho_\Gamma D_\Gamma \left(\frac{\partial^2\phi}{\partial x_i\partial x_j}\bigg|_{\mathbf{x}_\beta}^{(1)} - \frac{\partial^2\phi}{\partial x_i\partial x_j}\bigg|_{\mathbf{x}_\alpha}^{(1)} \right) \left(S_i^{(\alpha\beta)} - \epsilon^{(\alpha\beta)}\Delta x_i{}^{(\alpha\beta)} \right) \Delta x_j{}^{(\alpha\beta)} + \frac{1}{2}\rho_\Gamma D_\Gamma \left(\frac{\partial^2\phi}{\partial x_i\partial x_j}\bigg|_{\mathbf{x}_\alpha}^{(1)} + \frac{\partial^2\phi}{\partial x_i\partial x_j}\bigg|_{\mathbf{x}_\beta}^{(1)} \right) S_{i,j}^{(\alpha\beta,\Gamma)}. \end{aligned} \tag{51}$$

For the case of variable density and diffusion coefficients, we approximate the interface values with $\rho_\Gamma = (\overline{\rho}_\alpha + \overline{\rho}_\beta)/2$ and $D_\Gamma = (\overline{D}_\alpha + \overline{D}_\beta)/2$. Similar to convective fluxes, we utilize the deferred-correction approach for an efficient implicit discretization of the diffusive fluxes. Hence, Eq. (51) is split in two parts: A low-order term $F_{D,LO}^{(\alpha\beta)}$ and an high-order term $F_{D,HO}^{(\alpha\beta)}$. The former only involves the volume-averages that are captured in the first term on the right of Eq. (51) and is defined by

$$F_{D,LO}^{(\alpha\beta)} = \epsilon^{(\alpha\beta)}\rho_\Gamma D_\Gamma \left(\overline{\phi}_\beta - \overline{\phi}_\alpha \right). \tag{52}$$

The high-order term is obtained by subtracting $F_{D,LO}^{(\alpha\beta)}$ from $F_D^{(\alpha\beta)}$.

2.4. The k-exact projection scheme

In the following section, we will apply the spatial discretization method from Section 2.3 to the iterative projection method from Section 2.2. This basically involves the volumetric averaging of the different equations of the projection step and applying the k-exact reconstruction to it. We assume the volume-averages of the various field variables for time level t_n to be known. The density is approximated at the next time step using Eq. (7), where volumetric averaging leads to:

$$\overline{\rho}_\alpha^0 = \overline{\rho}_\alpha^n - \frac{\Delta t}{|\Omega_\alpha|} \sum_{\beta\in\{\beta_\alpha^{(1)}\}} (\dot{m}^n)^{(\alpha\beta,\Gamma)}. \tag{53}$$

The mass fluxes $\dot{m}^{(\alpha\beta,\Gamma)}$ at the element surfaces are calculated from Eq. (37). The thermochemical transport equations are subsequently solved as a coupled system of equations, that is written in the following:

$$\left(\frac{|\Omega_\alpha|\overline{\rho}_\alpha^m}{\Delta t} \right) \overline{h}_\alpha^{m+1} + \sum_{\beta\in\{\beta_\alpha^{(1)}\}} \frac{1}{2}\left[F_C^{(\alpha\beta)}\left(h^{m+1}\right) + F_D^{(\alpha\beta)}\left(h^{m+1}\right) \right] = \overline{\left(RHS_h\right)}_\alpha, \tag{54a}$$

$$\left(\frac{|\Omega_\alpha|\overline{\rho}_\alpha^m}{\Delta t} \right) \overline{Y}_{s,\alpha}^{m+1} + \sum_{\beta\in\{\beta_\alpha^{(1)}\}} \frac{1}{2}\left[F_C^{(\alpha\beta)}\left(Y_s^{m+1}\right) + F_D^{(\alpha\beta)}\left(Y_s^{m+1}\right) \right] - \frac{1}{2}\overline{\dot{\omega}}_{s,\alpha}^{m+1} = \overline{\left(RHS_{Y_s}\right)}_\alpha. \tag{54b}$$

Here, the volume-averaged right-hand side terms are given by

$$\overline{\left(RHS_h\right)}_\alpha = \frac{|\Omega_\alpha|\overline{\rho}_\alpha^n\overline{h}_\alpha^n}{\Delta t} - \sum_{\beta\in\{\beta_\alpha^{(1)}\}} \frac{1}{2}\left[F_C^{(\alpha\beta)}(h^n) + F_D^{(\alpha\beta)}(h^n) \right], \tag{55a}$$

$$\overline{\left(RHS_{Y_s}\right)}_\alpha = \frac{|\Omega_\alpha|\overline{\rho}_\alpha^n\overline{Y}_{s,\alpha}^n}{\Delta t} - \sum_{\beta\in\{\beta_\alpha^{(1)}\}} \frac{1}{2}\left[F_C^{(\alpha\beta)}\left(Y_s^n\right) + F_D^{(\alpha\beta)}\left(Y_s^n\right) \right] + \frac{1}{2}\overline{\dot{\omega}}_{s,\alpha}^n. \tag{55b}$$

Eq. (54) is transformed to a linear system of equations $\mathbf{Ax} = \mathbf{b}$, which is solved using the Biconjugate Gradient Stabilized (BiCGSTAB) method [64]. Here, $\mathbf{x}$ represents the solution vector with entries $\overline{h}_\alpha^{m+1}$ and $\overline{Y}_{s,\alpha}^{m+1}$ to be determined. The sparse matrix $\mathbf{A}$ results from the implicit fluxes and source terms, whereas the vector of the right-hand side $\mathbf{b}$ is calculated from explicit components. As mentioned above, a fully implicit treatment of the fluxes $F_C^{(\alpha\beta)}(\phi^{m+1})$ and $F_D^{(\alpha\beta)}(\phi^{m+1})$ requires a costly update of all flow gradients during the sub-iterations of the iterative solution method. To save computing time, we utilize the deferred correction approach [61,62] where a flux $F^{(\alpha\beta)}(\phi^{m+1})$ is split in two parts $\widetilde{F}^{(\alpha\beta)}$ and $\hat{F}^{(\alpha\beta)}$. The former part $\widetilde{F}^{(\alpha\beta)}$ corresponds to a low-order flux formulation, which only requires information from immediate neighboring elements. In contrast, a higher order of accuracy can be realized with the latter part $\hat{F}^{(\alpha\beta)}$. The splitting allows us to calculate any implicit flux through [61,62]

$$F^{(\alpha\beta)}\left(\phi^{m+1}\right) = \widetilde{F}^{(\alpha\beta)}\left(\phi^{m+1}\right) + \left[\hat{F}^{(\alpha\beta)}(\phi^n) - \widetilde{F}^{(\alpha\beta)}(\phi^n) \right], \tag{56}$$

where the computationally expensive flux $\hat{F}^{(\alpha\beta)}$ only needs to be calculated in an explicit manner. This significantly reduces the computing time to solve the system of equations. The components $\widetilde{F}^{(\alpha\beta)}$ and $\hat{F}^{(\alpha\beta)}$ are selected in such a way that we obtain the following implicit fluxes:

$$F_C^{(\alpha\beta)}\left(\phi^{m+1}\right) = F_{C,LO}^{(\alpha\beta)}\left(\phi^{m+1}\right) + F_{C,HO}^{(\alpha\beta)}(\phi^n) \qquad \text{and} \qquad F_D^{(\alpha\beta)}\left(\phi^{m+1}\right) = F_{D,LO}^{(\alpha\beta)}\left(\phi^{m+1}\right) + F_{D,HO}^{(\alpha\beta)}(\phi^n). \tag{57}$$

After solving the system of Eq. (54), the updated density $\overline{\rho}_\alpha^{m+1}$ and temperature $\overline{T}^{m+1}$ are calculated using the volume-averaged Eq. (11). However, we simply use the primitive volume-averages, which introduces the spatial error described in Eq. (30). Similar errors arise in the volumetric averaging of the chemical source term $\overline{\dot{\omega}}_{s,\alpha}$ and for the volumetric averaging of time derivatives. This error is accepted in favor of the complexity of our method. Otherwise it would require a more frequent update of flow gradients and thus cause a massive increase in computing time.

The updated density field is used to solve for the volume-averaged intermediate velocity field $\overline{\mathbf{u}}^*$ by solving the discretized momentum equations:

$$\left(\frac{|\Omega_\alpha|\overline{\rho}_\alpha^{m+1}}{\Delta t}\right)\overline{u}_{i,\alpha}^* + \sum_{\beta\in\{\beta_\alpha^{(1)}\}}\frac{1}{2}\left[F_C^{(\alpha\beta)}\left(u_i^*\right) + F_D^{(\alpha\beta)}\left(u_i^*\right)\right] = \overline{\left(RHS_{u_i}\right)}_\alpha. \tag{58}$$

The right-hand side is given by

$$\overline{\left(RHS_{u_i}\right)}_\alpha = \frac{|\Omega_\alpha|\overline{\rho}_\alpha^n\overline{u}_{i,\alpha}^n}{\Delta t} - \sum_{\beta\in\{\beta_\alpha^{(1)}\}}\frac{1}{2}\left[F_C^{(\alpha\beta)}\left(u_i^n\right) + F_D^{(\alpha\beta)}\left(u_i^n\right)\right] + |\Omega_\alpha|\overline{\left(\frac{\partial p_\mathrm{d}}{\partial x_i}\right)}_\alpha^n. \tag{59}$$

Analogous to the thermochemical transport, we use the deferred correction approach to compute the implicit fluxes $F_C^{(\alpha\beta)}\left(u_i^*\right)$ and $F_D^{(\alpha\beta)}\left(u_i^*\right)$. The volume-averaged dynamic pressure gradient $\overline{(\partial p_\mathrm{d}/\partial x_i)}_\alpha^n$ is calculated by a sum of k-exact fluxes of p_d^n over the element surfaces, which is given for $k = 2$ by

$$\overline{\left(\frac{\partial p_\mathrm{d}}{\partial x_i}\right)}_\alpha^n = \frac{1}{|\Omega_\alpha|}\sum_{\beta\in\{\beta_\alpha^{(1)}\}}\left(p_\mathrm{d}^n\Big|_{\mathbf{x}_\Gamma}^{(3)}S_i^{(\alpha\beta)} + \frac{\partial p_\mathrm{d}^n}{\partial x_j}\Big|_{\mathbf{x}_\Gamma}^{(2)}S_{i,j}^{(\alpha\beta)} + \frac{1}{2}\frac{\partial^2 p_\mathrm{d}^n}{\partial x_j\partial x_k}\Big|_{\mathbf{x}_\Gamma}^{(1)}S_{i,jk}^{(\alpha\beta)}\right) + \mathcal{O}\left(h^3\right). \tag{60}$$

The face values at the point $\mathbf{x}_\Gamma$ are calculated centrally from the reconstruction polynomials of the adjacent elements. It was shown in a previous work [4] that the accuracy of this term has a significant impact on the spatial accuracy on the entire projection step.

Once the intermediate velocity field $\overline{\mathbf{u}}_\alpha^*$ has been obtained from Eq. (58), it is used to update the intermediate mass fluxes $(\dot{m}^*)^{\alpha\beta,\Gamma}$ at the element interfaces using Eq. (37a). These terms then act as right-hand side for a discretized Poisson equation for the pseudo-pressure $\delta\overline{p}_\alpha = \overline{p}_\alpha^{n+1} - \overline{p}_\alpha^n$, which is obtained by averaging Eq. (15) volumetrically:

$$\sum_{\beta\in\{\beta_\alpha^{(1)}\}}F_D^{(\alpha\beta)}(\delta p) = \frac{1}{2\Delta t^2}\left(3\overline{\rho}_\alpha^{m+1} - 2\overline{\rho}_\alpha^n + \overline{\rho}_\alpha^{n-1}\right) + \frac{1}{\Delta t}\sum_{\beta\in\{\beta_\alpha^{(1)}\}}\left(\dot{m}^*\right)^{(\alpha\beta,\Gamma)}, \tag{61}$$

which also contains the time derivative of the density on the right-hand side. Due to the elliptical character of Eq. (61), we use the Flexible Generalized Minimal Residual (FGMRES) method with multi-grid preconditioning to solve for δp. Additionally, the Laplace fluxes $F_D^{(\alpha\beta)}(\delta p)$ are calculcated in a fully implicit manner, hence requiring significantly more computing time. For this reason, we calculate $F_D^{(\alpha\beta)}(\delta p)$ always with a 1-exact accuracy, even if higher accuracy levels are used for the other field variables. This significantly reduces the computing time since we do not require a frequent update of the Hessian of δp within each Krylov sub-iteration. A previous study [4] also showed that the solution accuracy is only marginally affected by this treatment of δp compared to a fully implicit 2-exact discretization.

The pseudo-pressure gradient is used to update the mass fluxes $(\dot{m}^{m+1})^{(\alpha\beta,\Gamma)}$ for the next sub-iteration. This is done by enforcing Eq. (17) on the element surfaces $A_{\alpha\beta}$:

$$\iint_{A_{\alpha\beta}}\left(\rho^{m+1}u_i^{m+1}\right)n_i\,\mathrm{d}A = \iint_{A_{\alpha\beta}}\left(\rho^{n+1}u_i^*\right)n_i\,\mathrm{d}A - \Delta t\iint_{A_{\alpha\beta}}\left(\frac{\partial\,\delta p}{\partial x_i}\right)n_i\,\mathrm{d}A, \tag{62}$$

which corresponds to $(\dot{m}^{m+1})^{(\alpha\beta,\Gamma)} = (\dot{m}^*)^{(\alpha\beta,\Gamma)} - \Delta t\,F_D^{(\alpha\beta)}(\delta p)$. Hence, the updated mass fluxes are determined by subtracting the introduced pseudo-pressure Laplace flux. This indirectly enforces the continuity equation on the element surfaces, which was found to suppress the emergence of parasitic error modes, especially for variable-density flow problems and with a collocated variable arrangement in space and time.

Once all sub-iterations have been carried out, the approximate velocity field $\overline{u}_{i,\alpha}^*$ and the old pressure $\overline{p}_\alpha^n$ are updated to the next time level t_{n+1} through the volume-averaged Eq. (13)

$$\overline{\left(\rho^{n+1}u_i^{n+1}\right)}_\alpha = \overline{\left(\rho^{n+1}u_i^*\right)}_\alpha - \Delta t\overline{\left(\frac{\partial\delta p}{\partial x_i}\right)}_\alpha \qquad \text{and} \qquad \overline{p}_\alpha^{n+1} = \overline{p}_\alpha^n + \overline{\left(\frac{\partial\delta p}{\partial x_i}\right)}_\alpha, \tag{63}$$

where the averaged pseudo-pressure gradient is calculated according to Eq. (60). The velocity correction still contains the averaged conservative variables $\overline{(\rho u_i)}_\alpha$, which cannot be replaced by their primitive counterparts $\overline{\rho}_\alpha\overline{u}_{i,\alpha}$ without sacrificing spatial accuracy when reconstructing with $k = 2$. To counteract this, we use Eq. (30) to derive the following correction term

$$\overline{u}_{i,\alpha}^{n+1} = \overline{u}_{i,\alpha}^* - \frac{\Delta t}{\overline{\rho}_\alpha^{n+1}}\overline{\left(\frac{\partial\delta p}{\partial x_i}\right)}_\alpha + \frac{1}{\overline{\rho}_\alpha^{n+1}}\frac{\partial\rho^{n+1}}{\partial x_j}\Big|_{\mathbf{x}_\alpha}\left(\frac{\partial u_i^{n+1}}{\partial x_k}\Big|_{\mathbf{x}_\alpha} - \frac{\partial u_i^*}{\partial x_k}\Big|_{\mathbf{x}_\alpha}\right)\left(\mathcal{M}_{j,\alpha}\mathcal{M}_{k,\alpha} - \mathcal{M}_{jk,\alpha}\right) + \mathcal{O}\left(h^3\right), \tag{64}$$

which, however, requires the gradient of the final velocity field $\partial u_i^{n+1}/\partial x_i\big|_{\mathbf{x}_\alpha}$. We can obtain an expression for this variable by enforcing Eq. (13) at locations $\mathbf{x}_\alpha$

$$\rho^{n+1}\big|_{\mathbf{x}_\alpha} u_i^{n+1}\big|_{\mathbf{x}_\alpha} = \rho^{n+1}\big|_{\mathbf{x}_\alpha} u_i^{*}\big|_{\mathbf{x}_\alpha} - \Delta t \left.\frac{\partial \delta p}{\partial x_i}\right|_{\mathbf{x}_\alpha} \tag{65}$$

and by taking the spatial derivative of this relation, which leads to the following relation:

$$\rho^{n+1}\big|_{\mathbf{x}_\alpha}\left(\left.\frac{\partial u_i^{n+1}}{\partial x_k}\right|_{\mathbf{x}_\alpha} - \left.\frac{\partial u_i^{*}}{\partial x_k}\right|_{\mathbf{x}_\alpha}\right) = \left.\frac{\partial \rho^{n+1}}{\partial x_k}\right|_{\mathbf{x}_\alpha}\left(u_i^{*}\big|_{\mathbf{x}_\alpha} - u_i^{n+1}\big|_{\mathbf{x}_\alpha}\right) - \Delta t \left.\frac{\partial^2 \delta p}{\partial x_i \partial x_k}\right|_{\mathbf{x}_\alpha} \tag{66}$$

Dividing by the point-valued density $\rho^{n+1}\big|_{\mathbf{x}_\alpha}$ and substituting the difference of velocities $(u_i^{*}\big|_{\mathbf{x}_\alpha} - u_i^{n+1}\big|_{\mathbf{x}_\alpha})$ via Eq. (65) finally results in an expression for the difference of the velocity gradients in Eq. (64)

$$\left(\left.\frac{\partial u_i^{n+1}}{\partial x_k}\right|_{\mathbf{x}_\alpha} - \left.\frac{\partial u_i^{*}}{\partial x_k}\right|_{\mathbf{x}_\alpha}\right) = \frac{\Delta t}{\rho^{n+1}\big|_{\mathbf{x}_\alpha}}\left(\frac{1}{\rho^{n+1}\big|_{\mathbf{x}_\alpha}}\left.\frac{\partial \rho^{n+1}}{\partial x_k}\right|_{\mathbf{x}_\alpha}\left.\frac{\partial \delta p}{\partial x_i}\right|_{\mathbf{x}_\alpha} - \left.\frac{\partial^2 \delta p}{\partial x_i \partial x_k}\right|_{\mathbf{x}_\alpha}\right), \tag{67}$$

which allows us to obtain the corrected velocity field $\bar{u}_{i,\alpha}^{n+1}$ at time level t_{n+1}. For clarification, an overview of the entire solution algorithm is given in Fig. 3.

3. Results

The proposed discretization method is verified and validated for two exactness levels $k = 1$ and $k = 2$. In the 1-exact method, the Green-Gauss gradient is corrected according to Eq. (25), without calculating higher-order derivatives. Consequently, the correction terms $F_{C,HO}^{(\alpha\beta)}$ and $F_{D,HO}^{(\alpha\beta)}$, used for the computation of convective and diffusive fluxes, are simplified. In contrast, the 2-exact method requires the computation of the Hessian matrix, as well as an additional correction step for the gradients. The calculations for the flux correction terms and the correction terms in the projection method follow the 2-exact formulations presented above. However, for the solution of the pressure correction equation, the Laplacian fluxes are computed using a 1-exact reconstruction, as discussed above. The high-order limitation approach is only applied to thermochemical field variables ρ, h and Y_s.

To assess the impact of the k-exact discretization on the numerical error, the test cases are also computed using conventional discretization methods. These schemes are characterized by a formal 0-exact reconstruction, meaning that no correction of the Green-Gauss gradients is applied. Depending on the test case, convective fluxes are either discretized using the Central Difference Scheme (CDS) or the Quadratic Upwind Difference Scheme [65] (QUDS). The latter is commonly referred to as quadratic upwind interpolation for convection kinematics (QUICK) scheme. The CDS method is consistently used for flux calculations in the momentum conservation equations, without any limiter. This method is particularly known for its low numerical dissipation on Cartesian grids [66], though it tends to suffer from instability. For the discretization of enthalpy and species fluxes, the QUDS method is applied, in conjunction with the limiter approach by Venkatakrishnan [56]. This is necessary because the species and enthalpy transport equations in reactive flows require higher numerical dissipation to stabilize the solution due to large gradients near the flame front. The calculation of diffusive fluxes is performed using the method proposed by Mathur and Murthy [32] given above, without applying the derived k-exact corrections.

For all three methods considered, the BiCGSTAB algorithm with Jacobi preconditioning is used to solve all transport equations. The Poisson equation is consistently solved using the FGMRES method, with a geometric multigrid preconditioning scheme implemented over three grid levels using a V-cycle. It is important to note that the solver ThetaCOM is limited to three-dimensional computational grids. Therefore, even for the one- and two-dimensional test cases, three-dimensional computational domains are defined. In these cases, the third spatial direction is resolved by a single element, and symmetry boundary conditions are applied to the plane.

3.1. Isochoric species convection

In this test case, we consider the isochoric transport of a hydrogen-oxygen (H_2/O_2) mixture, neglecting diffusive transport and chemical reaction. The mixture is advected through a periodic one-dimensional domain $\Omega \in [0, L]$ with a constant background velocity $u_1 = 1\,\mathrm{m/s}$ and a length scale $L = 1\,\mathrm{m}$. The initial species mass fraction profiles at $t = 0$ are given by

$$Y_{H_2}(x_1) = Y_{H_2,\mathrm{ref}} \exp\left[-\frac{(x_1 - x_{1,c})^2}{2\sigma^2}\right], \tag{68a}$$

$$Y_{O_2}(x_1) = 1 - Y_{H_2}(x_1), \tag{68b}$$

with $Y_{H_2,\mathrm{ref}} = 0.1$ and $\sigma = 0.05\,\mathrm{m}$. The initial temperature profile is defined according to

$$T(x_1) = \left(\frac{p_0}{\rho_{\mathrm{ref}} R_u}\right)\left[\frac{1}{M_{O_2}} + Y_{H_2}\left(\frac{1}{M_{H_2}} - \frac{1}{M_{O_2}}\right)\right]^{-1}. \tag{69}$$

with a uniform density $\rho_{\mathrm{ref}} = 0.2\,\mathrm{kg/m^3}$ and thermodynamic pressure $p_0 = 1\,\mathrm{atm}$. R_u, M_{O_2} and M_{H_2} define the universal gas constant, as well as the molecular weights of oxygen and hydrogen, respectively. The temperature field in this setup is designed to enforce a

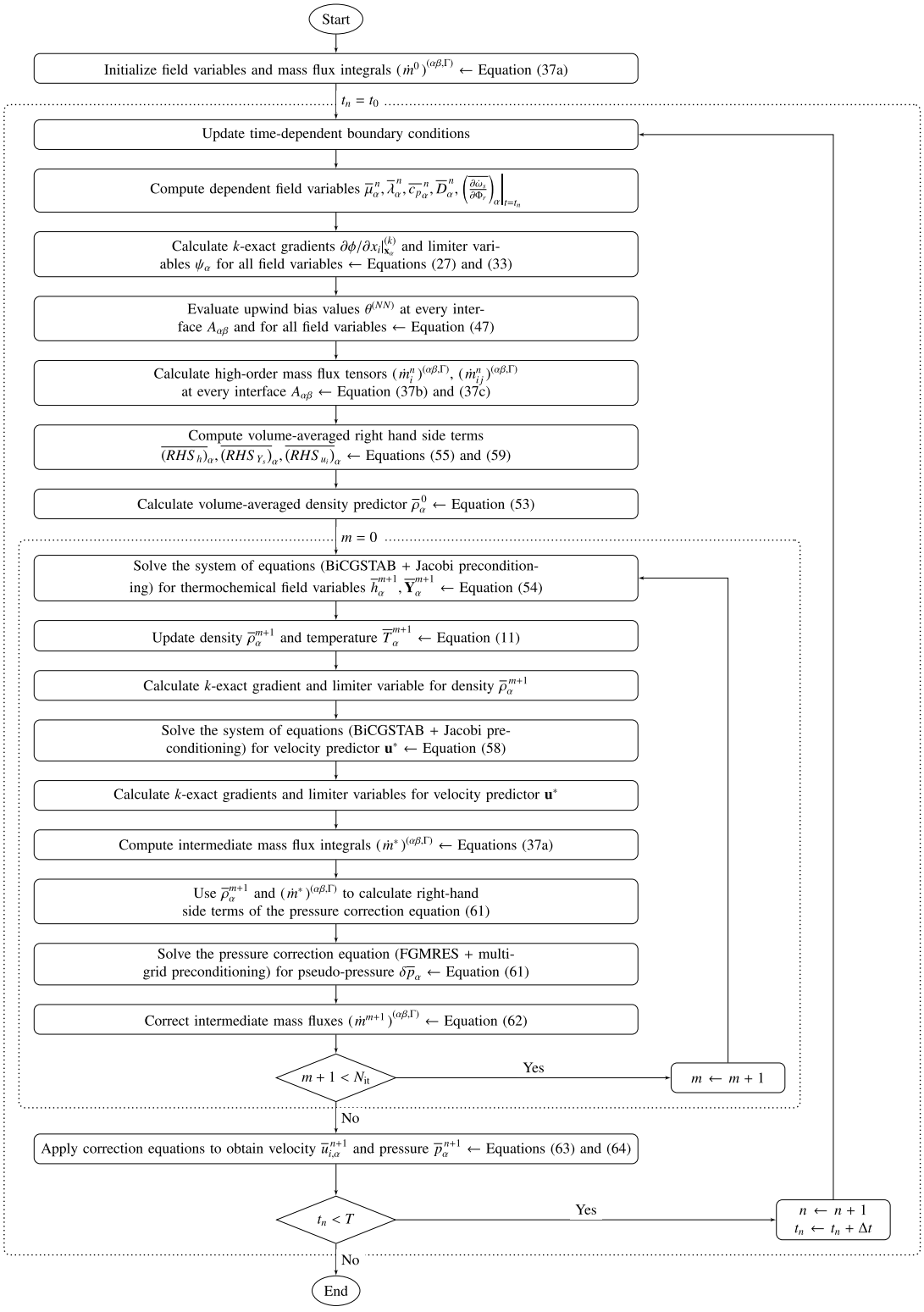

Fig. 3. Sequence diagram for an iterative projection step.

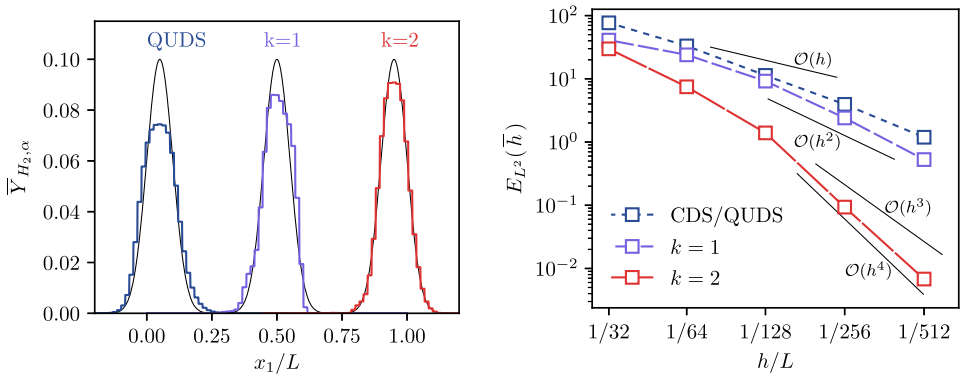

(a) Volume-averaged H_2-profiles. Black lines indicate the analytic solution.

(b) Spatial error convergence for $\overline{h}$. Black lines indicate orders of accuracy.

Fig. 4. Simulation results for the advection of an isochoric H_2/O_2 mixture.

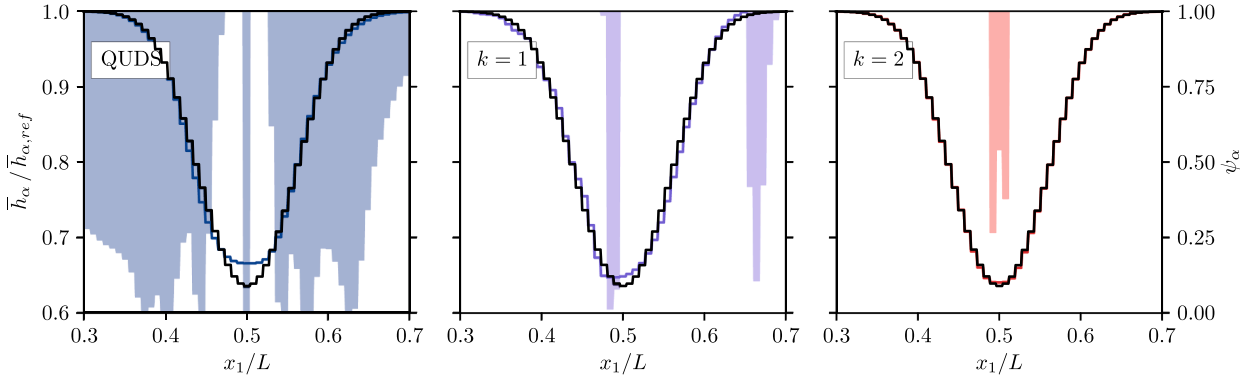

Fig. 5. Volume-averaged enthalpy profiles $\overline{h}_\alpha/\overline{h}_{\alpha,\mathrm{ref}}$ and corresponding limiter variables ψ_α for the advection of an isochoric H_2/O_2 mixture on a grid with $h = L/128$. The analytic solution (black solid line) is compared with the numerical solutions (colored lines). Shaded regions indicate the activation of the limiter, where $\psi < 1$.

constant density within Ω, ensuring that the velocity and pressure remain unaffected by variations in temperature and species mass fractions. As a result, this test case isolates the behavior of the species transport under idealized conditions, allowing us to evaluate the accuracy of the convective operator in a simplified yet relevant scenario for combustion applications. The profile of the mixture is advected by a distance $\delta = L$, where it should ideally preserve its initial shape. The calculations are performed on various grids with an average grid scale $h = \{L/32, L/64, L/128, L/256, L/512\}$.

Fig. 4(a) shows volume-averaged profiles for hydrogen mass fraction $\overline{Y}_{\mathrm{H}_2,\alpha}$, obtained after simulations with the three considered schemes on the grid with $h = L/64$. The respective profiles are shifted, for the sake of clarity. In all cases, the maxima of the analytic solution are undercut. The 2-exact scheme provides the best accuracy with respect to symmetry and preservation of the maxima, maintaining the original profile shape more effectively than the 1-exact scheme, with the conventional scheme showing the largest deviation from the initial solution. Fig. 4(b) shows the spatial error convergence for the mixture's volume-averaged enthalpy $\overline{h}_\alpha$ as the grid is refined. To assess the simulation results, the L^2-norm error E_{L^2} is calculated using the following equation:

$$E_{L^2}\left(\overline{\phi}_\alpha\right) = \left[\frac{\sum_{\alpha=1}^{N}\left(\overline{\phi}_\alpha - \overline{\phi}_\alpha^{\mathrm{ex}}\right)^2 |\Omega_\alpha|}{\sum_{\alpha=1}^{N}|\Omega_\alpha|}\right]^{1/2}, \tag{70}$$

with the exact solution $\overline{\phi}_\alpha^{\mathrm{ex}}$ and the number of primary grid points N. The error of the 2-exact method falls from the grid with $h = L/128$ even at a slightly higher rate than a third order. This is due to the central flux calculation in Eq. (38), which changes to a fourth order on Cartesian grids and in the limit of a vanishing upwind bias θ [5]. In contrast, both the 1-exact and conventional schemes show second-order accuracy. Notably, the 1-exact scheme reduces errors compared to the conventional scheme, indicating its improved performance in preserving the solution profile as the grid is refined.

To assess the performance of the proposed schemes in preserving solution quality and limiting behavior Fig. 5 presents the solutions for volume-average enthalpy $\overline{h}_\alpha$ profiles obtained with all considered schemes on a grid with $h = L/128$. The underlying shaded regions indicate the locations where the limiter variable ψ_α satisfies $\psi < 1$ and hence, where the limitation procedure is

active. The results demonstrate clear differences in the behavior of the limiters across the schemes. The conventional method exhibits a significantly larger share of limited elements, with limitation triggered even in smooth regions of the solution. This over-activation leads to increased numerical diffusion and noticeable distortion of the advected profile. In contrast, the 2-exact scheme shows superior accuracy, with minimal limiter activation. For this scheme, limited elements are confined to small regions near the extrema of the profile. No element is fully limited on either grid, highlighting the robustness of the modified limiting procedure. The 1-exact scheme exhibits intermediate behavior, with slightly more limited elements than $k = 2$, and a minor asymmetry in the solution profile. Notably, for $k = 1$, the limiter is also activated near $x/L \approx 0.65$, correlating with the observed asymmetry.

3.2. Pseudo-isentropic vortex convection

The spatial error order of the convective operator is often verified in the literature by the convection of an isentropic vortex. However, this represents a solution of the compressible Euler equations and is therefore not applicable for the solution method of this work. In the work by Gendre et al. [67], the derivation of an alternative test case was presented, for which the convective transport of a pseudo-isentropic vortex through an inviscid fluid at low Mach numbers is considered. This test case is used in the following to determine the spatial error order of the convective operator for the k-exact multi-correction methods. The initial solution of the pseudo-isentropic vortex is given by:

$$u_1(\mathbf{x}) = u_{1,0} - a_0\left(\frac{x_2}{R}\right)P(\mathbf{x}), \tag{71a}$$

$$u_2(\mathbf{x}) = u_{2,0} + a_0\left(\frac{x_1}{R}\right)P(\mathbf{x}), \tag{71b}$$

$$p(\mathbf{x}) = p_0 - \frac{1}{2}\gamma p_0\left[P^2(\mathbf{x}) - \frac{1}{4}P^4(\mathbf{x}) - \frac{1}{24}(\gamma-2)P^6(\mathbf{x})\right], \tag{71c}$$

$$\rho(\mathbf{x}) = \rho_0 - \frac{1}{2}\rho_0\left[P^2(\mathbf{x}) + \frac{1}{4}(\gamma-2)P^4(\mathbf{x}) + \frac{1}{24}(\gamma-2)(2\gamma-3)P^6(\mathbf{x})\right]. \tag{71d}$$

Here $r^2 = x_1^2 + x_2^2$ represents the radial coordinate and R the size scale of the vortex. The quantities a_0 and T_0 denote the speed of sound and the temperature of the uniform flow field. The perturbation function $P(\mathbf{x})$ is represented by a Gaussian function of the form

$$P(\mathbf{x}) = \kappa \exp\left(-\frac{r^2}{2R^2}\right) \tag{72}$$

where the parameter κ specifies the degree of disturbance and thus the vorticity. The vortex is driven by an inviscid fluid at ambient velocity $\mathbf{u}_0 = (50, 0)^{\mathrm{T}}\,\mathrm{m/s}$, temperature $T_0 = 300\,\mathrm{K}$ and pressure $p_0 = 100\,\mathrm{kPa}$. The composition of dry air is selected for the fluid, which results in the density $\rho_0 = 1.28286\,\mathrm{kg/m^3}$ and the speed of sound $a_0 = 344.108\,\mathrm{m/s}$ at ambient conditions. The strength and length of the vortex are specified by the parameters $\kappa = 0.1$ and $R = 0.005\,\mathrm{m}$. The vortex is placed in the center $\mathbf{x}_c = (L/2, L/2)^{\mathrm{T}}$ of a periodic domain $\Omega \in [0, L] \times [0, L]$ and is convected over a distance $\delta x = L$, where $L = 0.1\,\mathrm{m}$. Hence, the vortex passes through the entire domain and should return to its starting position. The simulations are carried out on five fully unstructured triangular grids, where the average grid scale varies between $L/16$ and $L/256$. Fig. 6(a) shows an exemplary grid along with the initial solution for the x_2-velocity field.

First, this test case is used to analyze how the number of sub-iterations in the projection method influences the temporal error. Fig. 6(b) demonstrates the error convergence for the velocity component u_1, with results calculated using the 2-exact scheme on the

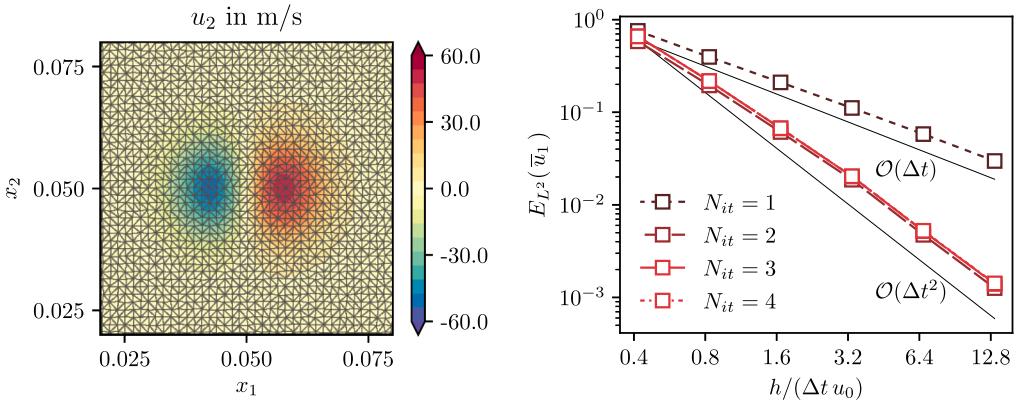

(a) Initial solution for x_2-velocity and unstructured primary grid with $h = L/128$.

(b) Temporal error convergence for velocity component $\overline{u}_1$. Straight black lines denote orders of accuracy.

Fig. 6. Setup for the pseudo-isentropic vortex advection test case and temporal error convergence for the 2-exact scheme with varying numbers of projection step sub-iterations.

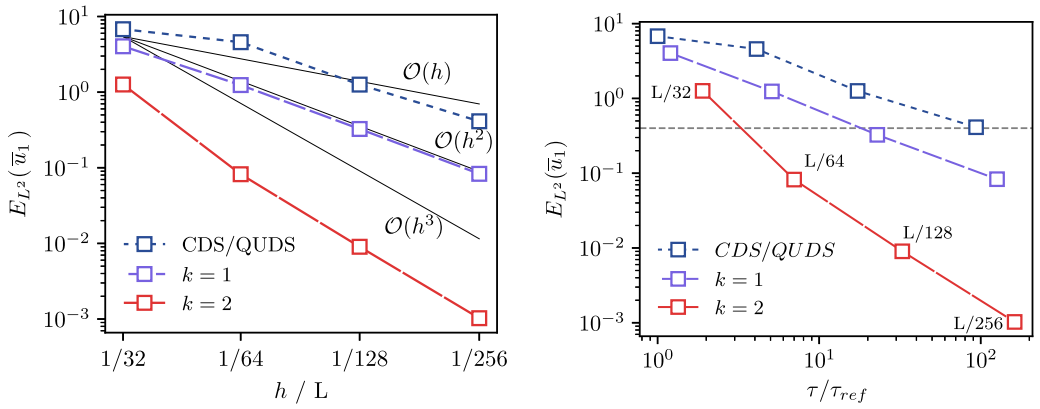

(a) x_1-velocity $\overline{u}_1$

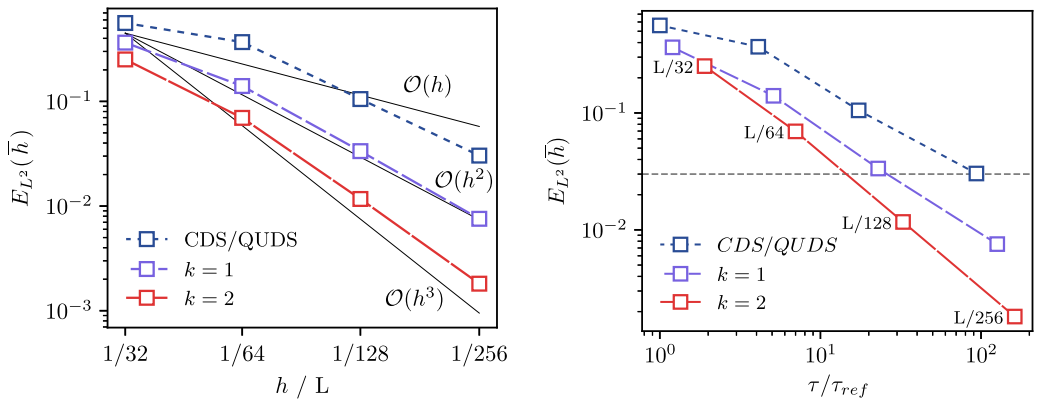

(b) Enthalpy $\overline{h}$

Fig. 7. Spatial error convergence (left) and performance results (right) for the pseudo-isentropic vortex advection test case.

finest grid, as the time step size is progressively reduced. A single sub-iteration produces first-order accuracy, while two or more iterations yield second-order accuracy. As noted by Pierce [16], increasing the number of iterations beyond two does not improve overall accuracy but influences the method's stability. Similar findings were observed for other spatial schemes and are omitted for clarity.

Based on these observations, two sub-iterations ($N_{\text{it}} = 2$) were selected for all subsequent simulations as a practical trade-off between accuracy and computational cost. It should also be noted that while a fixed number of sub-iterations suffices for the cases considered in this work, configurations involving extreme density variations or highly stiff source terms may benefit from a higher N_{it} to enhance robustness. Alternatively, the introduction of an adaptive stopping criterion based on residual convergence could provide additional efficiency by dynamically adjusting the number of iterations. Exploring such an adaptive strategy is an interesting path for future work.

Fig. 7 shows the spatial error convergence for the three spatial schemes in terms of x_1-velocity and enthalpy, using two sub-iterations. The time step Δt was chosen to ensure a sufficiently small CFL number $\sigma = 0.03$, minimizing the influence of temporal discretization errors and allowing a clearer comparison of spatial accuracy across the schemes. The 2-exact scheme achieves third-order spatial accuracy for the convective operator, despite grid irregularities. The other two schemes demonstrate second-order spatial accuracy, with the 1-exact scheme significantly reducing overall error compared to the conventional scheme.

Both k-exact schemes result in higher computational costs per iteration, as can be observed on the right of Fig. 7, where the same spatial errors are shown over the reduced computing time τ/τ_{ref} for a single iteration of each scheme. The latter is calculated with the calculation time τ_{ref}, which stems from one iteration with the CDS/QUDS scheme on the coarsest grid.

On average, the 1-exact method increases iteration time by 25 %, and the 2-exact method by 75 %, compared to the conventional scheme. Nevertheless, for a given error threshold, the k-exact schemes can greatly reduce overall computational time. For example, if an error threshold 0.4 is set for the velocity component u_1 (as indicated by the grey dashed line), the 2-exact method can cut computation time by 90 %, owing to the coarser grid allowed while maintaining the time step. Since the coarser grid also permits a fourfold increase in time step (due to the CFL condition), total time savings can reach 95 %. Similarly, the 1-exact method reduces computing time by 75 % with the same time step and up to 85 % with an adjusted time step.

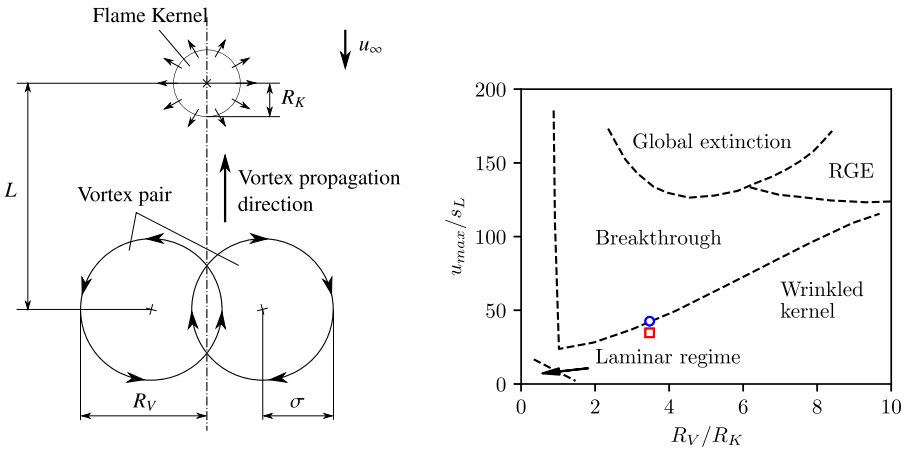

Fig. 8. Test case setup for the flame kernel-vortex interaction in a premixed H_2-air mixture (left) and flame regimes of the test case according to Vasudeo et al. [70] (right). The abbreviation RGE denotes the regeneration after general extinction regime. The red, square symbol indicates the simulated regime from the work of Vasudeo et al. whereas the blue, round symbol represents the regime position of this work. (For interpretation of the references to color in this figure legend, the reader is referred to the web version of this article.)

Table 1
Initial temperature and gas composition for the flame kernel-vortex interaction test case.

Gas state	T	Y_{H_2}	Y_{O_2}	Y_{N_2}	Y_{H_2O}	Y_{OH}	Y_O
Unburned	300.00 K	0.01885	0.14958	0.83157	–	–	–
Burned	1907.42 K	–	0.00320	0.83174	0.16445	0.00054	0.00001

3.3. Flame kernel-vortex interaction

Next, we consider an ignited flame kernel within a premixed hydrogen-air mixture interacting with a two-dimensional vortex pair. This interaction causes folding and stretching of the flame front, which can be classified into distinct regimes that have been studied both experimentally and numerically in several works [68–70].

Fig. 8 illustrates a schematic of the test case, along with various flame regimes for the flame kernel-vortex interaction, adapted from the work of Vasudeo et al. [70]. The simulation takes place within a two-dimensional domain of dimensions $3\,\text{cm} \times 4\,\text{cm}$. At the start, a counter-rotating vortex pair is initialized using two superimposed Lamb-Oseen vortex models [71], whose velocity fields overlap along the central axis of the simulation domain. The tangential velocity of a vortex is defined by Kolera-Gokula and Echekki [69], Vasudeo et al. [70]

$$u_{\tan}(\mathbf{x}) = \begin{cases} \frac{\psi}{2\pi r}\left[1 - \exp\left(-\frac{r^2}{\sigma^2}\right)\right] & \text{for} \quad r \leq \sigma, \\ 0 & \text{for} \quad r > \sigma, \end{cases} \tag{73}$$

where $r = \sqrt{(x_1 - x_{1,c})^2 + (x_2 - x_{2,c})^2}$ is the radial distance, $\sigma = 1.5\,\text{mm}$ is the vortex length scale, ψ represents the vortex strength, and the initial vortex centers are located at $\mathbf{x}_c = [\pm 1\,\text{mm}, -1.5\,\text{mm}]^\text{T}$. The chosen values for σ and $\mathbf{x}_c$ yield an outer vortex radius of $R_V = 2.5\,\text{mm}$. It is worth noting that Eq. (73) presents a discontinuity at $r = \sigma$, which may introduce parasitic pressure modes during the simulation. To avoid discontinuities in the velocity field, the vortex field in our work is multiplied by a continuous function $H(r)$, defined as

$$H(r) = 1 - \frac{1}{2}\left[1 + \tanh\left(\frac{r - (1+\epsilon)\sigma}{(1-\epsilon)\sigma}\right)\right], \tag{74}$$

where the parameter ϵ controls the smoothness of the transition and is set to $\epsilon = 0.3$. This results in the following modified velocity field:

$$u_{\tan}(\mathbf{x}) = \frac{\psi}{2\pi r} H(r)\left[1 - \exp\left(-\frac{r^2}{\sigma^2}\right)\right]. \tag{75}$$

This modification eliminates the discontinuity at $r = \sigma$, creating a smooth vortex field, which is used as initial condition for the test case.

The vortex strength is given by $\psi \approx 9.9399 \cdot \sigma \cdot u_{\max}$, where the maximum tangential velocity is set to $u_{\max} = 40\,\text{m/s}$ at $r = \sigma$. The flame kernel, with a radius $R_K = 0.72\,\text{mm}$, is positioned at a distance of $L = 3\,\text{mm}$ from the vortex pair. The initial temperature and

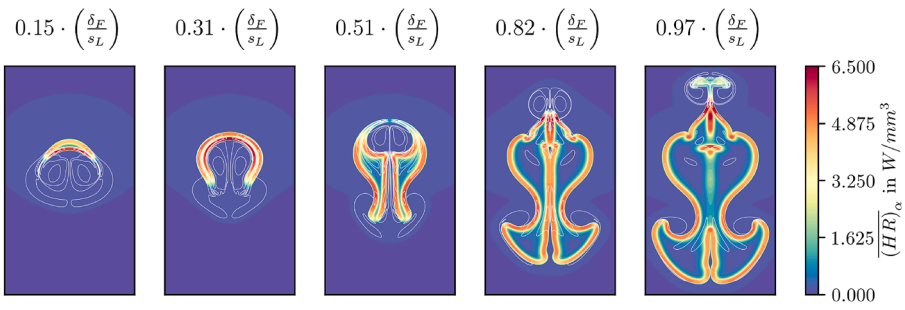

Fig. 9. Volume-averaged heat release $\overline{(HR)}_\alpha$ at different times of the flame kernel-vortex interaction, calculated on the reference grid with 1536×2048 vertices. White lines indicated the normalized vorticity $\omega \cdot (\delta_F / s_L) \in \{10, 20, 40, 80, 160\}$.

gas composition of the flame kernel are detailed in Table 1, based on the equilibrium state of the mixture after combustion in an isobaric reactor model. The enthalpy and species mass fractions are initialized using a Gaussian pulse function, which, for the species mass fractions Y_s, takes the form

$$Y_s = Y_{s,b} + \left(Y_{s,u} - Y_{s,b}\right) \exp\left(-\frac{r^2}{R_K^2}\right). \tag{76}$$

Here, r is the radial distance from the center of the flame kernel, $Y_{s,u}$ represents the mass fractions of the unburned gas, and $Y_{s,b}$ those of the burned gas. The unburned gas is a stoichiometric hydrogen-air mixture with a molar N_2/O_2 ratio of 6.35, and the ambient pressure is set to $p_0 = 1$ bar. To enhance convergence, a constant background velocity of $u_\infty = -2\,\mathrm{m/s}$ is added in the x_2-direction. The top and bottom edges of the domain are treated with inflow and outflow boundary conditions, while the lateral boundaries use periodic conditions.

With the given parameters for R_V, R_K and $u_{\max}$, the work by Vasudeo et al. shows flame kernel-vortex interaction in the "wrinkled kernel" regime. In this regime, the flame kernel is strongly deformed by the vortex pair without extinguishment, as indicated by the red symbol in Fig. 8. The regime position is influenced by both the velocity $u_{\max}$ and the laminar flame velocity s_L. Vasudeo et al. used the *GRI-Mech* 2.11 reaction mechanism [72], which predicts a flame speed of $s_L \approx 1.15\mathrm{m/s}$. In contrast, this work uses the more recent H_2 reaction mechanism by Ó Conaire [73] which comprises eight species and 19 elementary reactions, and which predicts a laminar flame speed $s_L = 0.9388\mathrm{m/s}$ and a flame thickness $\delta_F = 0.45793\mathrm{mm}$. This change in flame speed shifts the test case's regime in the diagram toward the "breakthrough regime" (shown by the blue symbol in Fig. 8), characterized by the flame kernel locally extinguishing and splitting due to the vortex interaction. However, these differences in the regimes are not critical for this study, as the data from Vasudeo et al. is insufficient to validate the higher-order schemes used here. Thus, a reference solution is generated for the parameters on a fine Cartesian grid with 1536×2048 vertices. This grid is sufficiently fine that differences between the discretization schemes are marginal. The objective is to assess whether the flame front propagation can be accurately captured on coarser grids using various spatial schemes. The flame-vortex interaction is simulated over the chemical timescale $(\delta_F / s_L) = 0.48778\mathrm{ms}$, with a time step of $\Delta t = 0.05\ \mu\mathrm{s}$ in the reference simulation.

Fig. 9 presents the volume-averaged heat release at selected points in time, calculated using the 2-exact discretization scheme. White iso-lines represent the vorticity ω, highlighting the location of the vortex pair. Initially, the vortex pair directly impacts the flame kernel, inducing a strong deformation that causes the flame front to spread in a horseshoe shape around the vortices. This interaction leads to the detachment of a second vortex pair in the opposite direction, expanding the lower section of the flame kernel. As the central vortex pair continues to exert significant momentum, it locally extinguishes the flame, splitting it into two distinct flame kernels at $t = 0.51 \cdot (\delta_F / s_L)$. After this extinction, hot exhaust gases are drawn back into the vortex pair, leading to the re-ignition of the mixture. Over time, the flame fronts from the two separate ignition points merge into a single flame kernel, which is evident at $t = 0.97 \cdot (\delta_F / s_L)$.

Fig. 10 displays the temporal trajectories of the integral mean values of vorticity $\overline{\omega}$ and the hydroperoxyl mass fraction $\overline{Y}_{HO_2}$, computed by integrating over the entire computational domain Ω

$$\overline{\omega}(t) = \frac{1}{|\Omega|} \iint_\Omega \omega(t) \mathrm{d}A \qquad \text{and} \qquad \overline{Y}_{HO_2}(t) = \frac{1}{|\Omega|} \iint_\Omega Y_{HO_2}(t) \mathrm{d}A. \tag{77}$$

The vorticity characterizes the flow field, while the hydroperoxyl radical represents an intermediate species indicating the progress of chemical reactions. Both characteristic curves will be used to evaluate the discretization schemes when the test case is reproduced on coarser computational grids. Initially, an increase in vorticity is observed up to $t \approx 0.45 \cdot (\delta_F / s_L)$, corresponding to the horseshoe-shaped deformation of the flame kernel. Following this, vorticity decreases due to the passage of the vortex through the ignition core, leading to local extinction of the flame front. At $t \approx 0.80 \cdot (\delta_F / s_L)$, vorticity increases again, marking the re-ignition phase. Unlike vorticity, the hydroperoxyl curve shows a steady increase throughout the simulation. The trajectories calculated from all three discretization schemes exhibit only minor differences, confirming that the grid used for the reference simulation is sufficiently fine. To validate this, an additional simulation was performed using the 2-exact method on an even finer grid, which revealed no further changes in the solution, reinforcing the adequacy of the chosen grid resolution.

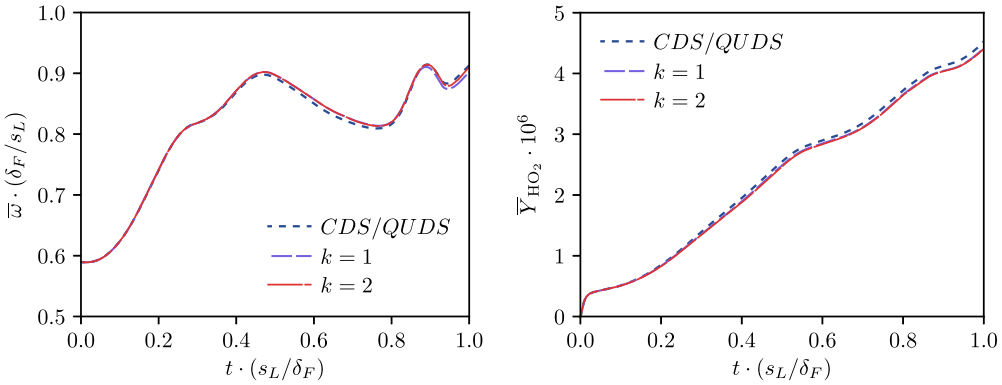

Fig. 10. Temporal evolution of the integral vorticity $\overline{\omega}$ and the integral hydroperoxyl mass fraction $\overline{Y}_{HO_2}$ during the flame kernel-vortex interaction calculated on the reference grid with 1536×2048 vertices.

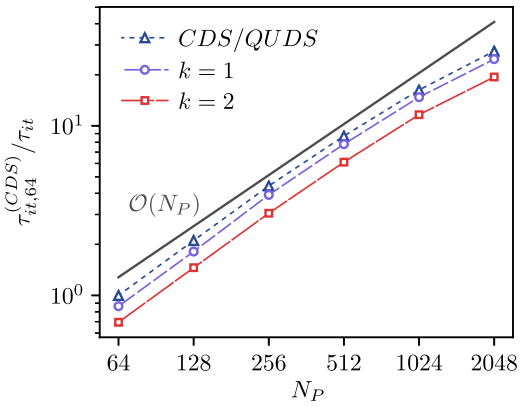

Fig. 11. Parallel speedup of the discretization methods for the flame kernel-vortex interaction on the reference grid with 1536×2048 primary grid vertices. τ_{it} refers to the average iteration time of the considered discretization schemes and $\tau_{it,64}^{(CDS)}$ is the iteration time of the CDS/QUDS scheme with 64 processors used as reference.

Parallel scalability is a key factor for evaluating the performance of the k-exact multiple-correction method. In the reference simulations, the computational grid includes 6.3 million nodes (taking the third dimension into account), providing a large number of degrees of freedom to assess scalability against the conventional scheme. To examine this, the average iteration time for each of the three schemes was measured as a function of the number of processors $N_P = \{64, 128, 256, 512, 1024, 2048\}$ over five independent simulation runs. Each run computed ten time steps of the test case with a constant five sub-iterations for the Krylov solver to maintain consistency. Fig. 11 presents the speedup, comparing the average iteration time $\tau_{it,64}^{(CDS)}$ of the CDS/QUDS method on 64 processors with the average iteration time τ_{it} of the other setups. The results demonstrate linear scaling across all methods up to $N_P = 1024$, after which the speedup begins to taper off slightly. This shows that the multiple-correction approach preserves parallel scalability, even with higher-order reconstructions. Although both k-exact methods exhibit higher iteration times than the conventional method, the increase is modest: about 10 % for $k = 1$ and 40 % for $k = 2$. This overhead is notably lower than in the previous non-reactive test case, likely due to the additional computational demand of the chemical source term, which diminishes the relative impact of k-exact corrections on the overall computation time.

Fig. 12(a) shows iso-lines of temperature at $T = 1192.4$ K, calculated using the three different schemes on a coarser grid and at time $t = 0.82 \cdot (\delta_F/s_L)$. For comparison, the gray solid iso-line represents the results from the 2-exact reference simulations using the finer grid. The coarser grid consists of 768×1024 nodes and hence half the resolution of the reference grid, resolving the flame thickness with 11.72 nodes. The simulation is carried out with a time step $\Delta t = 0.1$ μs, which is twice as large as in the reference simulation. Despite the lower resolution, both k-exact methods closely predict the flame shape, especially in regions of strong flame curvature. In contrast, the CDS/QUDS scheme shows larger deviations, particularly in these highly curved regions, indicating its reduced accuracy under such conditions. These errors become more pronounced on the even coarser grid with 384×512 nodes, as shown in Fig. 12(b). For the simulations on this grid, the time step has been further increased to $\Delta t = 0.2$ μs. Both k-exact methods show only slight deviations from the reference solution, which are within the error tolerance of the conventional method on the grid with 768×1024 nodes. The 2-exact method achieves the most accurate agreement, demonstrating its accuracy even with reduced grid resolution.

Fig. 13 shows the progression of integral vorticity, with the reference solution represented as a confidence band for comparison. The gray band indicates the envelope spanned by the minimum and maximum values of the three high-resolution solutions, while

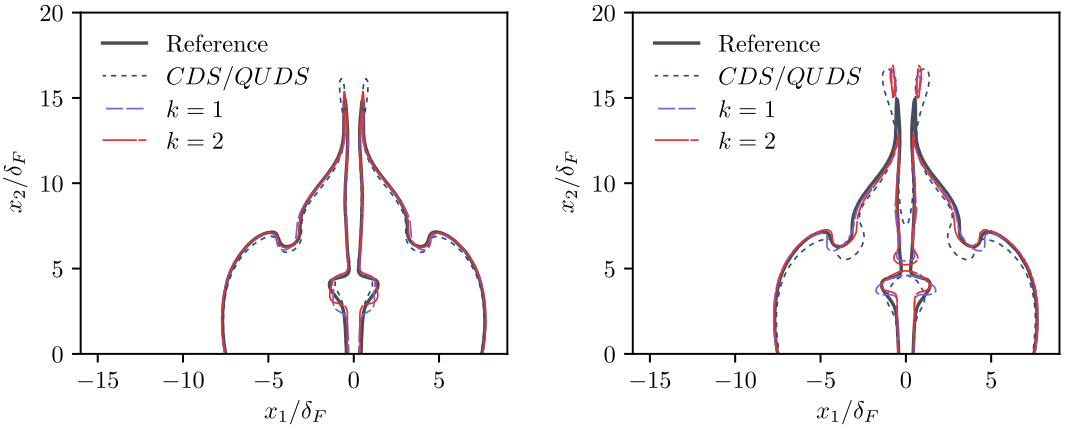

(a) 768 × 1024 vertices. (b) 384 × 512 vertices.

Fig. 12. Temperature iso-lines at $T = 1192.4$ K for the flame kernel-vortex interaction at time point $t = 0.82 \cdot (\delta_F / s_L)$, calculated with different grids and discretization schemes.

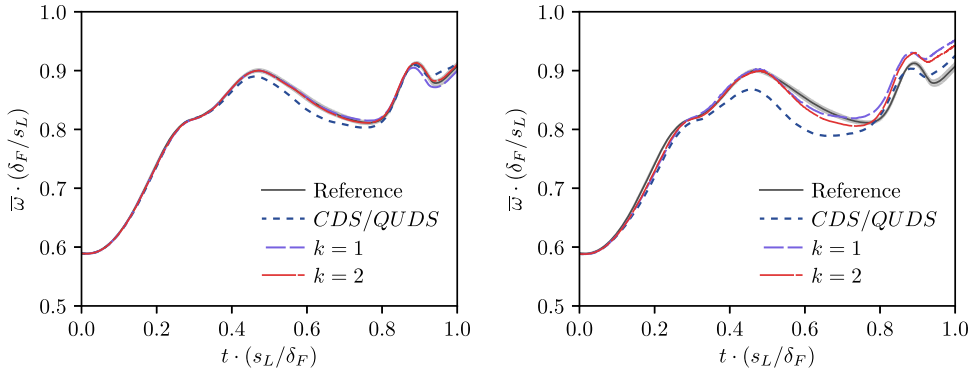

(a) 768 × 1024 vertices. (b) 384 × 512 vertices.

Fig. 13. Temporal evolution of the integral vorticity $\overline{\omega}$ for the flame-vortex interaction on coarser Cartesian grids.

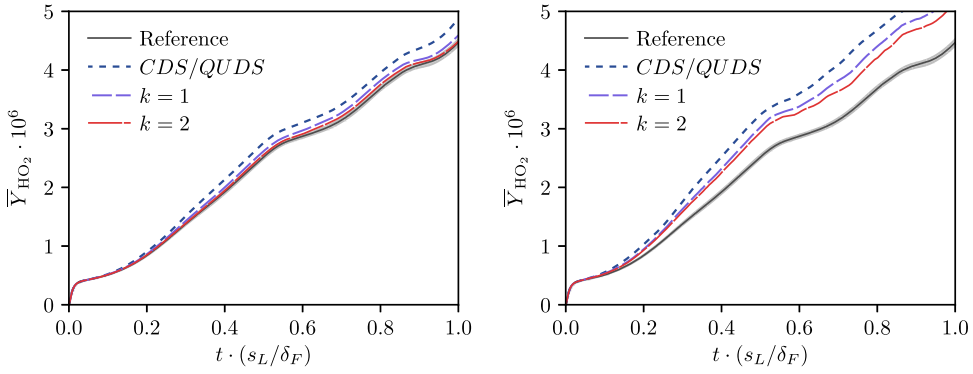

(a) 768 × 1024 vertices. (b) 384 × 512 vertices.

Fig. 14. Temporal evolution of the integral hydroperoxyl mass fraction $\overline{Y}_{HO_2}$ for the flame-vortex interaction on coarser Cartesian grids.

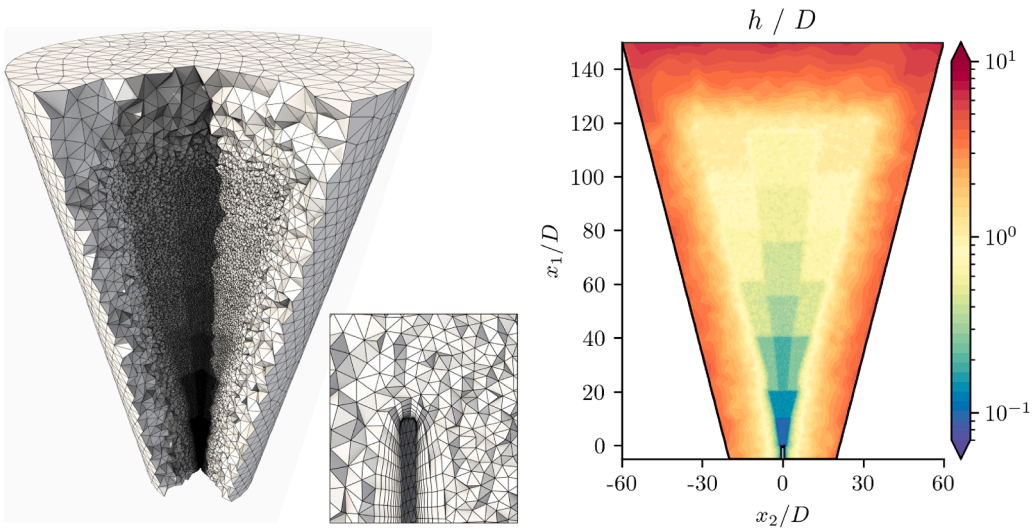

Fig. 15. Computational grid for the H3 flame test case.

the black line denotes their mean. This combined reference was adopted in place of a single high-order result (e.g., $k = 2$) to provide a more robust benchmark and to account for residual differences among the finest-grid solutions.

Both k-exact methods closely reproduce the reference simulations up to $t \approx 0.9(\delta_F/s_L)$, whereas the conventional discretization method shows noticeable deviations from the reference between $0.4(\delta_F/s_L) < t < 0.7(\delta_F/s_L)$. On the even coarser grid in Fig. 13(b), the conventional scheme exhibits even larger deviations, whereas both k-exact schemes capture the reference trajectory with minor differences up to $t \approx 0.8(\delta_F/s_L)$. A similar behavior is observed for the hydroperoxyl mass fraction in Fig. 14. On the grid with 768×1024 nodes, the trajectory is predicted almost identically using the 2-exact method, followed by the 1-exact method, which slightly overestimates the mass fraction. In contrast, the curve for the conventional method rises too steeply starting at $t \approx 0.2(\delta_F/s_L)$. On the coarsest grid, the mass fraction is overestimated by all three schemes, although the 2-exact method still yields the smallest errors. The results indicate that for both k-exact schemes, the solution quality on the 768×1024 grid remains largely consistent with that of the fine reference grid, whereas the conventional method already shows significant deviations at the same resolution. This suggests that higher-order schemes can achieve comparable accuracy on a coarser grid while substantially reducing computational costs. Considering the use of a larger time step on the coarse grid for comparability between different resolutions, the computational effort is reduced by 73.1 % with $k = 2$ and by 77.1 % with $k = 1$ compared to the conventional approach on the fine reference grid. If the same time step were used for both grid resolutions, the reduction in computational effort would be 47.4 % with the 2-exact scheme and 54.3 % with the 1-exact scheme.

3.4. H3 flame

The H3 flame is a standard benchmark for non-premixed flame modeling and has been extensively studied in previous work [74–80]. The burner consists of an 8, mm fuel nozzle supplying a diluted H_2/N_2 jet at $U = 34.8$, m/s, surrounded by a 140, mm coaxial air coflow at 0.2, m/s. Both streams enter at 300, K and atmospheric pressure. Optical measurements of this configuration provide high-quality experimental data for validation [81,82].

The test case is used to demonstrate the capability of the proposed multiple-correction scheme and the iterative projection method for simulating complex turbulent flames. The simulation domain, with a length of $155D$, is discretized predominantly using tetrahedral elements, as shown in Fig. 15. Despite its simple geometry, a fully unstructured grid is used to highlight the flexibility of the approach for complex large-eddy simulation test cases. The average grid scale h of the elements increases with distance to the fuel nozzle and the burner main axis, as indicated in Fig. 15. A time-varying turbulent velocity profile is imposed at the fuel inlet, which has been extracted from a turbulent pipe flow precursor simulation. Prismatic elements are used in the vicinity of the fuel nozzle walls, as shown in Fig. 15, to realize a sufficient boundary layer resolution. The primary grid comprises 1,056,108 nodes and 6,145,732 elements. An outlet boundary condition is used at the upper boundary of the computational domain, whereas an inlet boundary condition with the velocity and fluid composition of the air coflow is imposed at the conical side surfaces. Similar to the previous test case, the H_2 reaction mechanism by Ó Conaire [73] is utilized. In the context of large-eddy simulations, the governing Eq. (1) are solved in a Favre-filtered framework [83–85]. The Wall Adapting Local Eddy Viscosity (WALE) model [86] is used to take the influence of unresolved turbulent scales on the resolved flow field into account. The corresponding model constant C_W is set to a value of 0.5. In addition, an assumed probability density function model is used to model the influence of turbulence-chemistry interaction on the chemical source term [87,88]. The latter requires us to solve additional transport equations for the temperature variance and the turbulent scalar energy, both of which are treated in a similar fashion as the remaning thermochemical state variables. Assuming an optically thin medium, radiative heat losses are included by an additional source term $\dot{q}_{\text{rad}} = -4\sigma_s T^4 \epsilon$ applied to the enthalpy

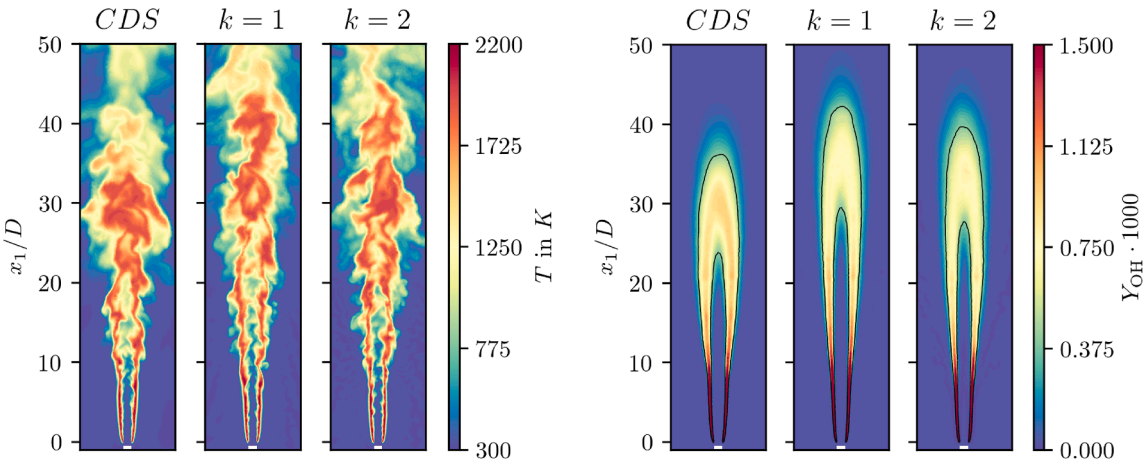

Fig. 16. Instantaneous temperature (left) and temporally averaged OH mass fraction for the H3 flame test case, calculated with the considered discretization schemes.

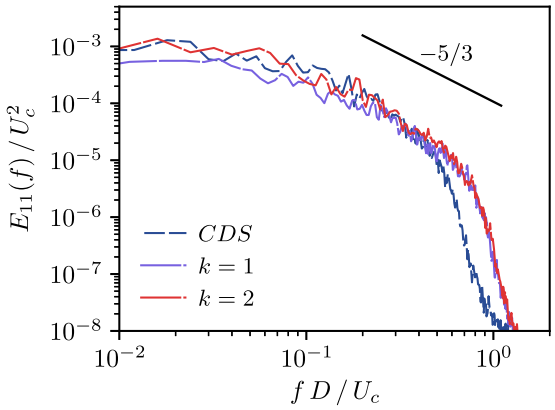

Fig. 17. One-dimensional energy spectra $E_{11}(f)$ on the main axis of the H3 flame, extracted at $x_1/D = 20$.

transport equation, where σ_s is the Stefan-Boltzmann constant and ϵ is the emissivity factor [89,90]. The simulations are performed with both proposed k-exact schemes and the CDS/QUDS scheme already used in the previos test case. For the sake of brevity, the latter is referred to as "CDS" in some figures. For all schemes, the limiting approach is only applied to the thermochemical state variables h and Y_s, whereas for pressure and velocities no limitation was required. A simulation is initialized with a starting solution of a fully developed flame, resulting from a former LES of the test case. First, the flame is simulated for 0.035 s, in order to account for effects from the initialization, followed by a temporal averaging of the flow variables for further 0.965 s. A time step of $\Delta = 1\,\mu$s is used in all simulation.

The left of Fig. 16 displays instantaneous, Favre-filtered temperature fields in the $x_1 - x_2$ plane, calculated through the utilized discretization schemes. A characteristic feature of the test case is the region $x_1/D \leq 15$, where unburned fuel interacts with the surrounding airflow. In this upstream zone, mixing is partially driven by molecular diffusion [75,91]. Beyond $x_1/D > 15$, however, turbulent transport becomes the dominant mixing mechanism [75,81]. This transition is captured in all simulations, although the CDS/QUDS method produces coarser coherent structures starting from approximately $x_1/D \approx 15$ onward compared to both k-exact approaches. Additionally, the high-order schemes exhibit enhanced transport of hot temperature regions, resulting in elevated temperatures downstream of $x_1/D > 40$. The differences in flame structure become even more pronounced when considering the time-averaged OH mass fraction, shown on the right of Fig. 16. The extent of the reaction zone is indicated by the black iso-line, corresponding to a time-averaged mass fraction of $\langle Y_{\mathrm{OH}} \rangle = 0.0004$. The CDS/QUDS scheme yields a shorter and broader reaction zone, marked by elevated $\langle Y_{\mathrm{OH}} \rangle$ values relative to those produced by the k-exact methods. Furthermore, for the 1-exact case, the reaction zone extends slightly farther downstream than for the 2-exact case.

Fig. 17 shows one-dimensional energy spectra calculated from the axial velocity $E_{11}(f)$ [85]

$$E_{11}(f) = \frac{1}{\pi} \int_{-\infty}^{\infty} \langle u_1(t) u_1(t+\tau) \rangle \exp\left(-2\pi I f \tau\right) \mathrm{d}\tau. \tag{78}$$

The spectra are calculated from temporal signals of u_{ax} extracted at the location $x_1/D = 20$ on the flame axis. The mean axial centerline velocity U_c at the corresponding location is used for normalization. In all three simulations, a characteristic $-5/3$ slope is observed,

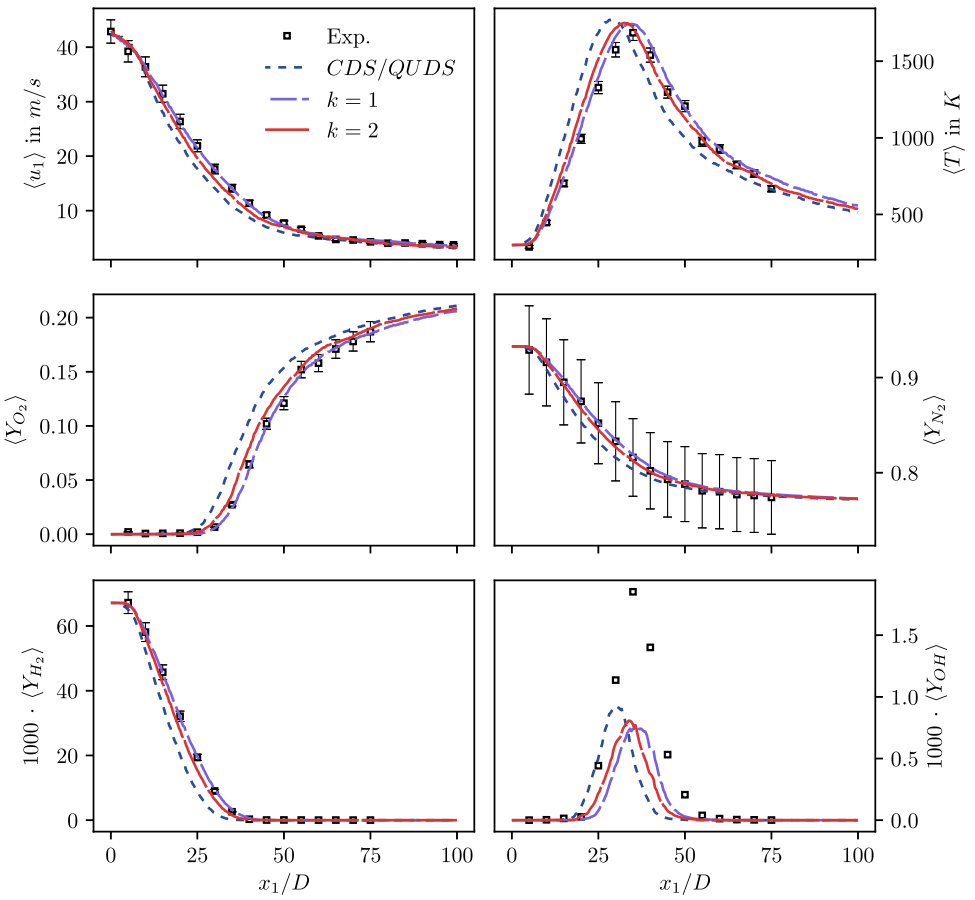

Fig. 18. Time-averaged mean profiles of selected field quantities along the main axis of the H3 flame. Experimental measurements are taken from Cheng et al.[82] and Meier et al.[81].

indicating the inertial subrange where energy cascades towards smaller scales at a constant rate [85]. However, both k-exact schemes resolve this range with finer scales compared to the conventional CDS/QUDS discretization, which is consistent with the presence of smaller coherent structures in the temperature fields shown in Fig. 16.

Time-averaged axial profiles of velocity $\langle u_1 \rangle$, temperature $\langle T \rangle$, and species mass fractions $\langle Y_{O_2} \rangle$, $\langle Y_{N_2} \rangle$, $\langle Y_{H_2} \rangle$, and $\langle Y_{OH} \rangle$ are shown in Fig. 18, alongside corresponding RMS fluctuations in Fig. 19. All profiles are extracted along the centerline of the flame in the axial direction. Experimental data from Cheng et al.[82] and Meier et al.[81] are included for comparison, with error bars shown in selected plots to indicate measurement uncertainty. All simulation results represent Favre-filtered quantities, with notation omitted for clarity.

The comparison reveals that the conventional CDS/QUDS scheme exhibits the largest deviations from experimental data across nearly all quantities. Specifically, it predicts a more rapid decay of the axial velocity $\langle u_1 \rangle$ and shows upstream displacements of the peak locations in the temperature and species profiles by approximately $5D$, indicating excessive scalar mixing and premature ignition. In terms of turbulence statistics, the CDS/QUDS scheme overestimates the axial turbulence intensity $\sqrt{\langle u_1' u_1' \rangle}/\langle u_1 \rangle$ by about 5 % in the region $10 < x_1/D < 20$, and the RMS fluctuations of O_2 and H_2 decay prematurely, deviating from the experimental trends by approximately $5D$. These observations are consistent with the right of Fig. 16, where the flame predicted by the CDS/QUDS scheme appears shorter and broader compared to those produced by the higher-order methods.

In contrast, both k-exact discretization schemes exhibit significantly improved agreement with the experimental data, underscoring their superior numerical accuracy and robustness towards grid distortions. Notably, the $k = 1$ scheme shows slightly better visual agreement in the upstream region ($x_1/D < 30$), particularly for mean velocity, temperature, and the mass fractions of major species. Beyond this region ($x_1/D > 30$), the $k = 2$ scheme more accurately captures mean temperature and certain fluctuation statistics, such as $\sqrt{\langle Y_{O_2}' Y_{O_2}' \rangle}$. However, the differences between the two k-exact schemes are relatively minor and largely within experimental uncertainty. Consequently, a definitive ranking of the two schemes cannot be established based solely on the current dataset. The axial turbulence intensity at the inlet ($x_1/D = 0$) is underpredicted by both k-exact schemes by approximately 5 % compared to experimental measurements. Nevertheless, this value aligns well with previous LES studies [77,79]. One area where both k-exact schemes show

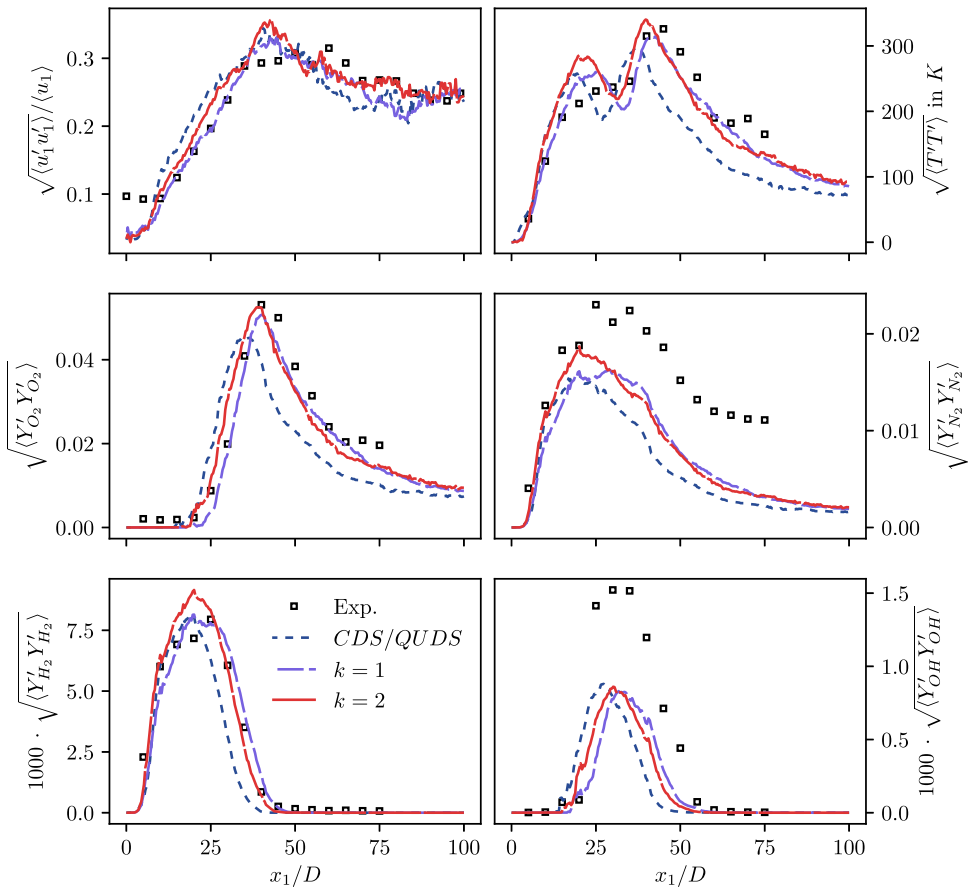

Fig. 19. Time-averaged fluctuation profiles of selected field quantities along the main axis of the H3 flame. Experimental measurements are taken from Cheng et al.[82] and Meier et al.[81].

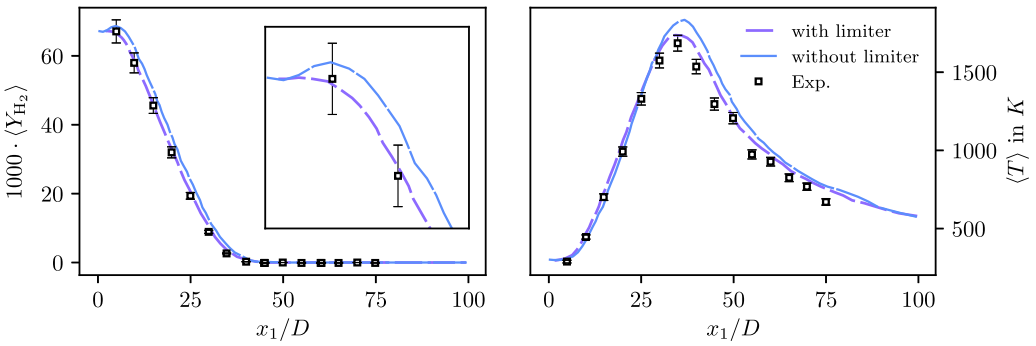

Fig. 20. Time-averaged mean profiles for hydrogen mass fraction $\langle Y_{H_2} \rangle$ and temperature $\langle T \rangle$ along the main axis of the H3 flame, calculated with the 1-exact scheme with (purple) and without limitation (blue) of thermochemical field variables. Experimental measurements are taken from Cheng et al.[82] and Meier et al.[81]. (For interpretation of the references to color in this figure legend, the reader is referred to the web version of this article.)

consistent discrepancies is the prediction of $\langle Y_{OH} \rangle$ and its RMS fluctuations in the flame front region. While the axial position of the peak values is accurately captured, the peak magnitudes are underpredicted. Similarly, RMS fluctuations of N_2 are underestimated for $x_1/D > 25$. These discrepancies persist even on a refined computational grid with approximately twice the number of degrees of freedom, which is not shown for brevity. This suggests that the errors are not primarily due to grid resolution. Instead, they may originate from limitations in turbulence–chemistry interaction modeling or deficiencies in the underlying chemical mechanism, which, for example, does not take the formation of nitric oxides into account.

To further assess the impact of the limitation strategy, an additional simulation has been performed with the 1-exact scheme without any limitation applied. The 1-exact scheme has been chosen due to computational constraints. However, the observed effects are expected to extend similarly to $k = 2$. Fig. 20 presents time-averaged axial profiles of the hydrogen mass fraction $\langle Y_{H_2} \rangle$ and temperature $\langle T \rangle$ along the burner centerline, comparing the limited and unlimited versions of the 1-exact scheme. The unlimited scheme exhibits a pronounced overshoot in $\langle Y_{H_2} \rangle$ near the region where the hydrogen jet interacts with the air coflow. Notably, the maximum mass fraction exceeds the core jet value, indicating an unphysical behavior. Analysis of instantaneous fields reveals that this artifact arises from local overshoots generated at the interface between the hydrogen jet and the coflow due to steep species gradients. These spurious local extrema accumulate during temporal averaging, resulting in the observed anomaly in the mean profile. The limited simulation effectively suppresses these overshoots, leading to a physically consistent decay of $\langle Y_{H_2} \rangle$ along the centerline and improved agreement with experimental measurements. A similar trend is observed for the temperature profile: the unlimited case produces an elevated peak temperature and a larger deviation from the experimental data, whereas the limited solution exhibits a reduced peak and better overall correspondence. The temperature overprediction in the unlimited case may stem from compounded thermochemical coupling effects amplified by the spurious species overshoots. Overall, these results emphasize the importance of robust limiting procedures in handling large thermochemical gradients without introducing non-physical artifacts.

4. Conclusion

In this work, the k-exact multiple-correction scheme for vertex-centered grids was applied, in conjunction with an iterative projection method, to solve transport equations for reactive flows in the low-Mach number regime. Implemented within the DLR ThetaCOM flow solver, this method demonstrates the potential of higher-order spatial discretization within an established production environment, preserving spatial accuracy through both 1- and 2-exact formulations. The results validate the advantages of the k-exact schemes over a conventional finite-volume method in terms of accuracy and computational efficiency. The 2-exact scheme achieved third-order spatial accuracy on fully unstructured grids, while the 1-exact scheme maintained second-order accuracy, both offering substantial improvements over the conventional discretization method.

In various test cases, the k-exact methods delivered significant computational savings over the conventional scheme. The test case of a pseudo-isentropic vortex transport revealed that two sub-iterations of the proposed iterative projection method were needed to sustain second-order temporal accuracy, highlighting the computational efficiency of the proposed solution algorithm. The method was particularly effective in simulating a flame kernel-vortex interaction, accurately capturing complex, transient reactive flow dynamics and proving its applicability to time-dependent reactive flows. Parallel scaling properties were comparable to those of the conventional scheme, confirming the approach's suitability for large-scale computations. Additionally, both k-exact schemes preserved the resolution of integral vorticity and hydroperoxyl mass fraction with half the grid resolution required by the conventional approach, reducing computational demands without compromising accuracy. Even at grid sizes further reduced, the k-exact method accurately maintained the vortex-flame kernel interaction, particularly with regard to integral vorticity, while the conventional scheme showed substantial deviations from reference results.

The simulation of a turbulent H_2/N_2-air diffusion flame aided as a comprehensive test for our proposed scheme to be used for large-eddy simulations of complex, turbulent combustion problems on fully unstructured grids. The results emphasized the limited predictive capability of the conventional scheme in capturing both mean and fluctuating fields of the reacting flow. Conversely, the k-exact schemes, including the $k = 1$ variant, provided substantial improvements and reliably reproduce key features of the flame. These findings highlight the effectiveness of high-order discretization methods for LES of complex, chemically reacting flows, and demonstrate that even lower-order implementations of the k-exact approach offer significant advantages over conventional schemes.

The proposed approach for the limitation in conjunction with adaptive numerical dissipation control demonstrated superior accuracy and robustness in all considered test cases. In the $1D$ advection test case, the k-exact schemes effectively preserved solution features and minimized unwanted limiter activation. In the turbulent H_2/N_2-air diffusion flame, the limiting approach suppressed unphysical species overshoots and clearly improved agreement with experimental data, highlighting its importance for maintaining physical fidelity in challenging reactive flow environments.

In conclusion, the proposed k-exact multiple-correction scheme provides not only enhanced accuracy but also significant efficiency benefits for simulating complex reactive flows on unstructured grids, establishing itself as a valuable tool for high-fidelity flow simulations in production-level computational environments. For future work, we aim to extend this k-exact approach to investigate its potential in enhancing the accuracy of turbulent reactive flow simulations in applications with complex geometries.

CRediT authorship contribution statement

Florian Setzwein: Writing – original draft, Visualization, Software, Methodology, Formal analysis, Conceptualization; **Peter Ess:** Writing – original draft, Supervision, Project administration, Methodology, Conceptualization; **Peter Gerlinger:** Writing – original draft, Supervision, Project administration, Methodology, Conceptualization.

Data availability

The authors do not have permission to share data.

Declaration of competing interest

The authors declare that they have no known competing financial interests or personal relationships that could have appeared to influence the work reported in this paper.

Acknowledgment

The authors gratefully acknowledge the scientific support and HPC resources provided by the German Aerospace Center (DLR). The HPC system CARO is partially funded by “Ministry of Science and Culture of Lower Saxony” and “Federal Ministry for Economic Affairs and Climate Action”. We would also like to thank Dr.-Ing. A. Fiolitakis for the helpful discussions on this work.

References

[1] J.A. Ekaterinaris, High-order accurate, low numerical diffusion methods for aerodynamics, Prog. Aerosp. Sci. 41 (3–4) (2005) 192–300.
[2] G. Pont, P. Brenner, P. Cinnella, B. Maugars, J.-C. Robinet, Multiple-correction hybrid k-exact schemes for high-order compressible RANS-LES simulations on fully unstructured grids, J. Comput. Phys. 350 (2017) 45–83.
[3] A. Menasria, P. Brenner, P. Cinnella, G. Pont, Toward an improved wall treatment for multiple-correction k-exact schemes, in: 2018 Fluid Dynamics Conference, AIAA 2018-4164, 2018.
[4] F. Setzwein, P. Ess, P. Gerlinger, An implicit high-order k-exact finite-volume approach on vertex-centered unstructured grids for incompressible flows, J. Comput. Phys. 446 (2021) 110629.
[5] F. Setzwein, P. Ess, P. Gerlinger, Adaptive numerical dissipation control for high-order k-exact reconstruction schemes on vertex-centered unstructured grids using artificial neural networks, J. Comput. Phys. 471 (2022) 111633.
[6] F. Setzwein, P. Ess, P. Gerlinger, Investigating the influence of a viscous flux correction for a high-Order k-Exact discretization scheme on unstructured grids, in: AIAA Scitech 2024 Forum, AIAA 2024-2175, 2024, p. 2175.
[7] F. Setzwein, M. Spraul, P. Ess, P.M. Gerlinger, On the structure of correction matrices for a k-exact high-order finite-volume scheme on vertex-centered unstructured grids, in: AIAA Scitech 2021 Forum, AIAA-2021-1548, 2021.
[8] F. Setzwein, P. Ess, P. Gerlinger, High-order k-exact finite volume scheme for vertex-centered unstructured grids, in: AIAA Scitech 2020 Forum, AIAA-2020-1785, 2020.
[9] L.Y.M. Gicquel, G. Staffelbach, T. Poinsot, Large eddy simulations of gaseous flames in gas turbine combustion chambers, Prog. Energy Combust. Sci. 38 (6) (2012) 782–817.
[10] B.W. Reuter, T.A. Oliver, R.D. Moser, A second-order-in-time, explicit approach addressing the redundancy in the low-Mach, variable-density Navier–Stokes equations, J. Comput. Phys. 514 (2024) 113216.
[11] A.S. Almgren, J.B. Bell, P. Colella, L.H. Howell, M.L. Welcome, A conservative adaptive projection method for the variable density incompressible Navier–Stokes equations, J. Comput. Phys. 142 (1) (1998) 1–46.
[12] J.B. Bell, D.L. Marcus, A second-order projection method for variable-density flows, J. Comput. Phys. 101 (2) (1992) 334–348.
[13] R. Knikker, A comparative study of high-order variable-property segregated algorithms for unsteady low Mach number flows, Int. J. Numer. Methods Fluids 66 (4) (2011) 403–427.
[14] J.F. MacArt, M.E. Mueller, Semi-implicit iterative methods for low Mach number turbulent reacting flows: operator splitting versus approximate factorization, J. Comput. Phys. 326 (2016) 569–595.
[15] R.B. Pember, L.H. Howell, J.B. Bell, P. Colella, W.Y. Crutchfield, W.A. Fiveland, J.P. Jessee, An adaptive projection method for unsteady, low-Mach number combustion, Combust. Sci. Technol. 140 (1–6) (1998) 123–168.
[16] C.D. Pierce, Progress-variable approach for large-eddy simulation of turbulent combustion, Ph.D. thesis, Stanford University, 2001.
[17] B. Savard, Y. Xuan, B. Bobbitt, G. Blanquart, A computationally-efficient, semi-implicit, iterative method for the time-integration of reacting flows with stiff chemistry, J. Comput. Phys. 295 (2015) 740–769.
[18] L. Shunn, F. Ham, Method of manufactured solutions applied to variable-density flow solvers, Annual Research Briefs-2007, Center for Turbulence Research (2007) 155–168.
[19] B. Lessani, M.V. Papalexandris, Time-accurate calculation of variable density flows with strong temperature gradients and combustion, J. Comput. Phys. 212 (1) (2006) 218–246.
[20] H.N. Najm, P.S. Wyckoff, O.M. Knio, A semi-implicit numerical scheme for reacting flow: I. Stiff chemistry, J. Comput. Phys. 143 (2) (1998) 381–402.
[21] F. Nicoud, Conservative high-order finite-difference schemes for low-Mach number flows, J. Comput. Phys. 158 (1) (2000) 71–97.
[22] J. Ventosa-Molina, J. Chiva, O. Lehmkuhl, J. Muela, C.D. Pérez-Segarra, A. Oliva, Numerical analysis of conservative unstructured discretisations for low Mach flows, Int. J. Numer. Methods Fluids 84 (6) (2017) 309–334.
[23] R. Yu, J. Yu, X.-S. Bai, An improved high-order scheme for DNS of low Mach number turbulent reacting flows based on stiff chemistry solver, J. Comput. Phys. 231 (16) (2012) 5504–5521.
[24] E. Motheau, J. Abraham, A high-order numerical algorithm for DNS of low-Mach-number reactive flows with detailed chemistry and quasi-spectral accuracy, J. Comput. Phys. 313 (2016) 430–454.
[25] O. Desjardins, G. Blanquart, G. Balarac, H. Pitsch, High order conservative finite difference scheme for variable density low mach number turbulent flows, J. Comput. Phys. 227 (15) (2008) 7125–7159.
[26] P. Trisjono, S. Kang, H. Pitsch, On a consistent high-order finite difference scheme with kinetic energy conservation for simulating turbulent reacting flows, J. Comput. Phys. 327 (2016) 612–628.
[27] M. Hassanaly, H. Koo, C.F. Lietz, S.T. Chong, V. Raman, A minimally-dissipative low-Mach number solver for complex reacting flows in OpenFOAM, Comput. Fluids 162 (2018) 11–25.
[28] Y. Cang, L. Wang, An improved fractional-step method on co-located unstructured meshes for weakly compressible flow simulations, Comput. Fluids 253 (2023) 105775.
[29] C.D. Pierce, P. Moin, Progress-variable approach for large-eddy simulation of non-premixed turbulent combustion, J. Fluid Mech. 504 (2004) 73–97.
[30] L. Shunn, F. Ham, Consistent and accurate state evaluations in variable-density flow simulations, Annual Research Briefs-2006, Center for Turbulence Research (2006) 135–147.
[31] L. Shunn, F. Ham, P. Moin, Verification of variable-density flow solvers using manufactured solutions, J. Comput. Phys. 231 (9) (2012) 3801–3827.
[32] S.R. Mathur, J.Y. Murthy, A pressure-based method for unstructured meshes, Numer. Heat Transf. 31 (2) (1997) 195–215.
[33] J.L. Thomas, B. Diskin, H. Nishikawa, A critical study of agglomerated multigrid methods for diffusion on highly-stretched grids, Comput. Fluids 41 (1) (2011) 82–93.
[34] H. Nishikawa, Beyond interface gradient: a general principle for constructing diffusion schemes, in: 40th Fluid Dynamics Conference and Exhibit, 2010, p. 5093. https://doi.org/10.2514/6.2010-5093
[35] F. Setzwein, P. Ess, P. Gerlinger, Investigating a high-order viscous flux scheme for unstructured grids, AIAA J. 62 (12) (2024) 4798–4811.
[36] H. Bijl, P. Wesseling, A unified method for computing incompressible and compressible flows in boundary-fitted coordinates, J. Comput. Phys. 141 (2) (1998) 153–173.

[37] A.W. Cook, J.J. Riley, Direct numerical simulation of a turbulent reactive plume on a parallel computer, J. Comput. Phys. 129 (2) (1996) 263–283.
[38] A. Majda, J. Sethian, The derivation and numerical solution of the equations for zero Mach number combustion, Combust. Sci. Technol. 42 (3–4) (1985) 185–205.
[39] C.-D. Munz, S. Roller, R. Klein, K.J. Geratz, The extension of incompressible flow solvers to the weakly compressible regime, Comput. Fluids 32 (2) (2003) 173–196.
[40] S. Gordon, B.J. McBride, Computer program for calculation of complex chemical equilibrium compositions, rocket performance, incident and reflected shocks, and Chapman–Jouguet detonations, Technical Report, 1976.
[41] S. Mathur, P.K. Tondon, S.C. Saxena, Thermal conductivity of binary, ternary and quaternary mixtures of rare gases, Mol. Phys. 12 (6) (1967) 569–579.
[42] M. Di Domenico, Numerical simulations of soot formation in turbulent flows, Ph.D. thesis, Universität Stuttgart, 2008.
[43] S.R. Turns, Introduction to Combustion Concepts and Applications, Mcgraw Hill Higher Education, 2011. Isbn 0071086870.
[44] T. Blacha, Effiziente Rußmodellierung in Laminaren und Turbulenten Flammen Unterschiedlicher Brennstoffe, Ph.D. thesis, Universität Stuttgart, 2012.
[45] J. Crank, P. Nicolson, A practical method for numerical evaluation of solutions of partial differential equations of the heat-conduction type, in: Mathematical Proceedings of the Cambridge Philosophical Society, 43, Cambridge University Press, 1947, pp. 50–67.
[46] T. Barth, D. Jespersen, The design and application of upwind schemes on unstructured meshes, in: 27th Aerospace Sciences Meeting, AIAA-89-0366, 1989.
[47] T. Barth, P. Frederickson, Higher order solution of the Euler equations on unstructured grids using quadratic reconstruction, in: 28th Aerospace Sciences Meeting, AIAA-90-0013, 1990.
[48] M.R.J. Charest, T.R. Canfield, N.R. Morgan, J. Waltz, J.G. Wohlbier, A high-order vertex-based central ENO finite-volume scheme for three-dimensional compressible flows, Comput. Fluids 114 (2015) 172–192.
[49] C.F. Ollivier-Gooch, Quasi-ENO schemes for unstructured meshes based on unlimited data-dependent least-squares reconstruction, J. Comput. Phys. 133 (1) (1997) 6–17.
[50] J.M. Pozo, M.-C. Villa-Uriol, A.F. Frangi, Efficient 3d geometric and zernike moments computation from unstructured surface meshes, IEEE Trans. Pattern Anal. Mach. Intell. 33 (3) (2011) 471–484.
[51] P. Koehl, Fast recursive computation of 3d geometric moments from surface meshes, IEEE Trans. Pattern Anal. Mach. Intell. 34 (11) (2012) 2158–2163.
[52] D. Gottlieb, C.-W. Shu, On the Gibbs phenomenon and its resolution, SIAM Rev. 39 (4) (1997) 644–668.
[53] H. Nishikawa, New unstructured-grid limiter functions, in: AIAA Scitech 2022 Forum, AIAA-2022-1374, 2022.
[54] S.A. Moe, J.A. Rossmanith, D.C. Seal, A simple and effective high-order shock-capturing limiter for discontinuous Galerkin methods, arXiv:1507.03024 (2015).
[55] C. Michalak, C. Ollivier-Gooch, Accuracy preserving limiter for the high-order accurate solution of the Buler equations, J. Comput. Phys. 228 (23) (2009) 8693–8711.
[56] V. Venkatakrishnan, Convergence to steady state solutions of the Euler equations on unstructured grids with limiters, J. Comput. Phys. 118 (1) (1995) 120–130.
[57] Z.J. Wang, A fast nested multi-grid viscous flow solver for adaptive cartesian/quad grids, Int. J. Numer. Methods Fluids 33 (5) (2000) 657–680.
[58] P. Tsoutsanis, Extended bounds limiter for high-order finite-volume schemes on unstructured meshes, J. Comput. Phys. 362 (2018) 69–94.
[59] P.D. Lax, Weak solutions of nonlinear hyperbolic equations and their numerical computation, Commun. Pure Appl. Math. 7 (1) (1954) 159–193.
[60] I. Mary, P. Sagaut, Large eddy simulation of flow around an airfoil near stall, AIAA J. 40 (6) (2002) 1139–1145.
[61] J.H. Ferziger, M. Perić, R.L. Street, Computational Methods for Fluid Dynamics, 3, Springer, 2002.
[62] P.K. Khosla, S.G. Rubin, A diagonally dominant second-order accurate implicit scheme, Comput. Fluids 2 (2) (1974) 207–209.
[63] H. Jasak, Error Analysis and Estimation for the Finite Volume Method with Applications to Fluid Flows, Ph.D. thesis, Imperial College London, 1996.
[64] H.A. Van der Vorst, Bi-CGSTAB: a fast and smoothly converging variant of Bi-CG for the solution of nonsymmetric linear systems, SIAM J. Sci. Stat. Comput. 13 (2) (1992) 631–644.
[65] B.P. Leonard, A stable and accurate convective modelling procedure based on quadratic upstream interpolation, Comput. Methods Appl. Mech. Eng. 19 (1) (1979) 59–98.
[66] S. Sarkar, Large eddy simulation of flows of engineering interest: a review, 50 Years of CFD in Engineering Sciences: A Commemorative Volume in Memory of D. Brian Spalding (2020) 363–400.
[67] F. Gendre, D. Ricot, G. Fritz, P. Sagaut, Grid refinement for aeroacoustics in the lattice Boltzmann method: a directional splitting approach, Phys. Rev. E 96 (2) (2017) 023311.
[68] D.A. Eichenberger, W.L. Roberts, Effect of unsteady stretch on spark-ignited flame kernel survival, Combust. Flame 118 (3) (1999) 469–478.
[69] H. Kolera-Gokula, T. Echekki, Direct numerical simulation of premixed flame kernel–vortex interactions in hydrogen–air mixtures, Combust. Flame 146 (1–2) (2006) 155–167.
[70] N. Vasudeo, T. Echekki, M.S. Day, J.B. Bell, The regime diagram for premixed flame kernel-vortex interactions–revisited, Phys. Fluids 22 (4) (2010) 043602.
[71] C.W. Oseen, Über die wirbelbewegung in einer reibenden flüssigkeit, Arkiv Mat., Astron. Fysik 7 (1912) 14–26.
[72] M. Frenklach, H. Wang, M. Goldenberg, G.P. Smith, D.M. Golden, C.T. Bowman, R.K. Hanson, W.C. Gardiner, V. Lissianski, GRI-Mech - An optimized detailed chemical reaction mechanism for methane combustion, Technical Report Technical Report No. GRI-95/0058, Gas Research Institute, 1995. http://www.me.berkeley.edu/gri_mech/.
[73] Ó.C. Marcus, H.J. Curran, J.M. Simmie, W.J. Pitz, C.K. Westbrook, A comprehensive modeling study of hydrogen oxidation, Int. J. Chem. Kinet. 36 (11) (2004) 603–622.
[74] R.S. Barlow, Proceedings of the international workshop on measurement and computation of turbulent nonpremixed flames, Technical Report, Sandia National Laboratories (SNL-CA), Livermore, CA (United States), 1996.
[75] A. D'Ausilio, I. Stankovic, B. Merci, Numerical study on the importance of the turbulent inlet boundary condition and differential diffusion in a turbulent H2/N2/air jet diffusion flame, Combust. Sci. Technol. 191 (1) (2019) 109–125.
[76] A. Fiolitakis, P.R. Ess, P. Gerlinger, M. Aigner, Modeling of heat transfer and differential diffusion in transported PDF methods, Combust. Flame 161 (8) (2014) 2107–2119.
[77] H. Forkel, J. Janicka, Large-eddy simulation of a turbulent hydrogen diffusion flame, Flow, Turbul. Combust. 65 (2000) 163–175.
[78] G. Maragkos, P. Rauwoens, B. Merci, Assessment of a methodology to include differential diffusion in numerical simulations of a turbulent flame, Int. J. Hydrogen Energy 40 (2) (2015) 1212–1228.
[79] B. Panjwani, A. Ertesvag, A. Gruber, K.E. Rian, Turbulence combustion closure model based on the eddy dissipation concept for large eddy simulation, Adv. Fluid Mech. VIII 69 (2010) 27–38.
[80] H. Pitsch, M. Chen, N. Peters, Unsteady flamelet modeling of turbulent hydrogen-air diffusion flames, in: Symposium (International) on Combustion, 27, Elsevier, 1998, pp. 1057–1064.
[81] W. Meier, S. Prucker, M.-H. Cao, W. Stricker, Characterization of turbulent H2/N2/air jet diffusion flames by single-pulse spontaneous Raman scattering, Combust. Sci. Technol. 118 (4–6) (1996) 293–312.
[82] T.-C. Cheng, G. Fruechtel, A. Neuber, F. Lipp, E.P. Hassel, J. Janicka, Experimental data base for numerical simulations of turbulent diffusion flames, Forsch. Ingenieurwes. 61 (1995) 165–171.
[83] P. Gerlinger, Numerische Verbrennungssimulation: Effiziente Numerische Simulation Turbulenter Verbrennung, Springer-Verlag, 2005.
[84] J. Froehlich, Large Eddy Simulation Turbulenter Stroemungen, 1, Springer, 2006.
[85] S.B. Pope, Turbulent Flows, Cambridge University Press, 2000.
[86] F. Ducros, F. Nicoud, T. Poinsot, Wall-adapting local eddy-viscosity models for simulations in complex geometries, Numer. Methods Fluid Dyn. VI (1998) 293–299.
[87] P. Gerlinger, Investigation of an assumed PDF approach for finite-rate chemistry, Combust. Sci. Technol. 175 (5) (2003) 841–872.

[88] S.S. Girimaji, Assumed β-pdf model for turbulent mixing: validation and extension to multiple scalar mixing, Combust. Sci. Technol. 78 (4–6) (1991) 177–196.
[89] F. Mauss, Entwicklung eines kinetischen Modells der Rußbildung mit schneller Polymerisation, Ph.D. thesis, RWTH Aachen, 1998.
[90] C. Eberle, P.M. Gerlinger, M. Aigner, Large eddy simulations of a sooting lifted turbulent jet-flame, in: 55th AIAA Aerospace Sciences Meeting, 2017, p. 1785.
[91] H. Pitsch, Unsteady flamelet modeling of differential diffusion in turbulent jet diffusion flames, Combust. Flame 123 (3) (2000) 358–374.